2011

Direct measurement of the mass difference between top and antitop quarks

V. M. Abazov
Joint Institute for Nuclear Research, Dubna, Russia

Kenneth A. Bloom
University of Nebraska - Lincoln, kbloom2@unl.edu

Daniel Claes
University of Nebraska - Lincoln, dclaes@unl.edu

Kayle DeVaughan
University of Nebraska - Lincoln

Aaron Dominguez
University of Nebraska-Lincoln, aarond@unl.edu

See next page for additional authors

Direct measurement of the mass difference between top and antitop quarks

V. M. Abazov,[35] B. Abbott,[73] B. S. Acharya,[29] M. Adams,[49] T. Adams,[47] G. D. Alexeev,[35] G. Alkhazov,[39] A. Alton,[61,*] G. Alverson,[60] G. A. Alves,[2] M. Aoki,[48] M. Arov,[58] A. Askew,[47] B. Åsman,[41] O. Atramentov,[65] C. Avila,[8] J. BackusMayes,[80] F. Badaud,[13] L. Bagby,[48] B. Baldin,[48] D. V. Bandurin,[47] S. Banerjee,[29] E. Barberis,[60] P. Baringer,[56] J. Barreto,[3] J. F. Bartlett,[48] U. Bassler,[18] V. Bazterra,[49] S. Beale,[6] A. Bean,[56] M. Begalli,[3] M. Begel,[71] C. Belanger-Champagne,[41] L. Bellantoni,[48] S. B. Beri,[27] G. Bernardi,[17] R. Bernhard,[22] I. Bertram,[42] M. Besançon,[18] R. Beuselinck,[43] V. A. Bezzubov,[38] P. C. Bhat,[48] V. Bhatnagar,[27] G. Blazey,[50] S. Blessing,[47] K. Bloom,[64] A. Boehnlein,[48] D. Boline,[70] E. E. Boos,[37] G. Borissov,[42] T. Bose,[59] A. Brandt,[76] O. Brandt,[23] R. Brock,[62] G. Brooijmans,[68] A. Bross,[48] D. Brown,[17] J. Brown,[17] X. B. Bu,[48] M. Buehler,[79] V. Buescher,[24] V. Bunichev,[37] S. Burdin,[42,†] T. H. Burnett,[80] C. P. Buszello,[41] B. Calpas,[15] E. Camacho-Pérez,[32] M. A. Carrasco-Lizarraga,[56] B. C. K. Casey,[48] H. Castilla-Valdez,[32] S. Chakrabarti,[70] D. Chakraborty,[50] K. M. Chan,[54] A. Chandra,[78] G. Chen,[56] S. Chevalier-Théry,[18] D. K. Cho,[75] S. W. Cho,[31] S. Choi,[31] B. Choudhary,[28] S. Cihangir,[48] D. Claes,[64] J. Clutter,[56] M. Cooke,[48] W. E. Cooper,[48] M. Corcoran,[78] F. Couderc,[18] M.-C. Cousinou,[15] A. Croc,[18] D. Cutts,[75] A. Das,[45] G. Davies,[43] K. De,[76] S. J. de Jong,[34] E. De La Cruz-Burelo,[32] F. Déliot,[18] M. Demarteau,[48] R. Demina,[69] D. Denisov,[48] S. P. Denisov,[38] S. Desai,[48] C. Deterre,[18] K. DeVaughan,[64] H. T. Diehl,[48] M. Diesburg,[48] P. F. Ding,[44] A. Dominguez,[64] T. Dorland,[80] A. Dubey,[28] L. V. Dudko,[37] D. Duggan,[65] A. Duperrin,[15] S. Dutt,[27] A. Dyshkant,[50] M. Eads,[64] D. Edmunds,[62] J. Ellison,[46] V. D. Elvira,[48] Y. Enari,[17] H. Evans,[52] A. Evdokimov,[71] V. N. Evdokimov,[38] G. Facini,[60] T. Ferbel,[69] F. Fiedler,[24] F. Filthaut,[34] W. Fisher,[62] H. E. Fisk,[48] M. Fortner,[50] H. Fox,[42] S. Fuess,[48] A. Garcia-Bellido,[69] V. Gavrilov,[36] P. Gay,[13] W. Geng,[15,62] D. Gerbaudo,[66] C. E. Gerber,[49] Y. Gershtein,[65] G. Ginther,[48,69] G. Golovanov,[35] A. Goussiou,[80] P. D. Grannis,[70] S. Greder,[19] H. Greenlee,[48] Z. D. Greenwood,[58] E. M. Gregores,[4] G. Grenier,[20] Ph. Gris,[13] J.-F. Grivaz,[16] A. Grohsjean,[18] S. Grünendahl,[48] M. W. Grünewald,[30] T. Guillemin,[16] F. Guo,[70] G. Gutierrez,[48] P. Gutierrez,[73] A. Haas,[68,‡] S. Hagopian,[47] J. Haley,[60] L. Han,[7] K. Harder,[44] A. Harel,[69] J. M. Hauptman,[55] J. Hays,[43] T. Head,[44] T. Hebbeker,[21] D. Hedin,[50] H. Hegab,[74] A. P. Heinson,[46] U. Heintz,[75] C. Hensel,[23] I. Heredia-De La Cruz,[32] K. Herner,[61] G. Hesketh,[44,§] M. D. Hildreth,[54] R. Hirosky,[79] T. Hoang,[47] J. D. Hobbs,[70] B. Hoeneisen,[12] M. Hohlfeld,[24] Z. Hubacek,[10,18] N. Huske,[17] V. Hynek,[10] I. Iashvili,[67] Y. Ilchenko,[77] R. Illingworth,[48] A. S. Ito,[48] S. Jabeen,[75] M. Jaffré,[16] D. Jamin,[15] A. Jayasinghe,[73] R. Jesik,[43] K. Johns,[45] M. Johnson,[48] D. Johnston,[64] A. Jonckheere,[48] P. Jonsson,[43] J. Joshi,[27] A. W. Jung,[48] A. Juste,[40] K. Kaadze,[57] E. Kajfasz,[15] D. Karmanov,[37] P. A. Kasper,[48] I. Katsanos,[64] R. Kehoe,[77] S. Kermiche,[15] N. Khalatyan,[48] A. Khanov,[74] A. Kharchilava,[67] Y. N. Kharzheev,[35] M. H. Kirby,[51] J. M. Kohli,[27] A. V. Kozelov,[38] J. Kraus,[62] S. Kulikov,[38] A. Kumar,[67] A. Kupco,[11] T. Kurča,[20] V. A. Kuzmin,[37] J. Kvita,[9] S. Lammers,[52] G. Landsberg,[75] P. Lebrun,[20] H. S. Lee,[31] S. W. Lee,[55] W. M. Lee,[48] J. Lellouch,[17] L. Li,[46] Q. Z. Li,[48] S. M. Lietti,[5] J. K. Lim,[31] D. Lincoln,[48] J. Linnemann,[62] V. V. Lipaev,[38] R. Lipton,[48] Y. Liu,[7] Z. Liu,[6] A. Lobodenko,[39] M. Lokajicek,[11] R. Lopes de Sa,[70] H. J. Lubatti,[80] R. Luna-Garcia,[32,‖] A. L. Lyon,[48] A. K. A. Maciel,[2] D. Mackin,[78] R. Madar,[18] R. Magaña-Villalba,[32] S. Malik,[64] V. L. Malyshev,[35] Y. Maravin,[57] J. Martínez-Ortega,[32] R. McCarthy,[70] C. L. McGivern,[56] M. M. Meijer,[34] A. Melnitchouk,[63] D. Menezes,[50] P. G. Mercadante,[4] M. Merkin,[37] A. Meyer,[21] J. Meyer,[23] F. Miconi,[19] N. K. Mondal,[29] G. S. Muanza,[15] M. Mulhearn,[79] E. Nagy,[15] M. Naimuddin,[28] M. Narain,[75] R. Nayyar,[28] H. A. Neal,[61] J. P. Negret,[8] P. Neustroev,[39] S. F. Novaes,[5] T. Nunnemann,[25] G. Obrant,[39,††] J. Orduna,[78] N. Osman,[15] J. Osta,[54] G. J. Otero y Garzón,[1] M. Padilla,[46] A. Pal,[76] N. Parashar,[53] V. Parihar,[75] S. K. Park,[31] J. Parsons,[68] R. Partridge,[75,‡] N. Parua,[52] A. Patwa,[71] B. Penning,[48] M. Perfilov,[37] K. Peters,[44] Y. Peters,[44] K. Petridis,[44] G. Petrillo,[69] P. Pétroff,[16] R. Piegaia,[1] M.-A. Pleier,[71] P. L. M. Podesta-Lerma,[32,¶] V. M. Podstavkov,[48] P. Polozov,[36] A. V. Popov,[38] M. Prewitt,[78] D. Price,[52] N. Prokopenko,[38] S. Protopopescu,[71] J. Qian,[61] A. Quadt,[23] B. Quinn,[63] M. S. Rangel,[2] K. Ranjan,[28] P. N. Ratoff,[42] I. Razumov,[38] P. Renkel,[77] M. Rijssenbeek,[70] I. Ripp-Baudot,[19] F. Rizatdinova,[74] M. Rominsky,[48] A. Ross,[42] C. Royon,[18] P. Rubinov,[48] R. Ruchti,[54] G. Safronov,[36] G. Sajot,[14] P. Salcido,[50] A. Sánchez-Hernández,[32] M. P. Sanders,[25] B. Sanghi,[48] A. S. Santos,[5] G. Savage,[48] L. Sawyer,[58] T. Scanlon,[43] R. D. Schamberger,[70] Y. Scheglov,[39] H. Schellman,[51] T. Schliephake,[26] S. Schlobohm,[80] C. Schwanenberger,[44] R. Schwienhorst,[62] J. Sekaric,[56] H. Severini,[73] E. Shabalina,[23] V. Shary,[18] A. A. Shchukin,[38] R. K. Shivpuri,[28] V. Simak,[10] V. Sirotenko,[48] P. Skubic,[73] P. Slattery,[69] D. Smirnov,[54] K. J. Smith,[67] G. R. Snow,[64] J. Snow,[72] S. Snyder,[71] S. Söldner-Rembold,[44] L. Sonnenschein,[21] K. Soustruznik,[9] J. Stark,[14] V. Stolin,[36] D. A. Stoyanova,[38] M. Strauss,[73] D. Strom,[49] L. Stutte,[48] L. Suter,[44] P. Svoisky,[73] M. Takahashi,[44] A. Tanasijczuk,[1] W. Taylor,[6] M. Titov,[18] V. V. Tokmenin,[35] Y.-T. Tsai,[69] D. Tsybychev,[70] B. Tuchming,[18] C. Tully,[66] L. Uvarov,[39] S. Uvarov,[39] S. Uzunyan,[50] R. Van Kooten,[52] W. M. van Leeuwen,[33] N. Varelas,[49] E. W. Varnes,[45] I. A. Vasilyev,[38] P. Verdier,[20] L. S. Vertogradov,[35] M. Verzocchi,[48] M. Vesterinen,[44] D. Vilanova,[18] P. Vokac,[10] H. D. Wahl,[47]

M. H. L. S. Wang,[48] J. Warchol,[54] G. Watts,[80] M. Wayne,[54] M. Weber,[48,**] L. Welty-Rieger,[51] A. White,[76] D. Wicke,[26] M. R. J. Williams,[42] G. W. Wilson,[56] M. Wobisch,[58] D. R. Wood,[60] T. R. Wyatt,[44] Y. Xie,[48] C. Xu,[61] S. Yacoob,[51] R. Yamada,[48] W.-C. Yang,[44] T. Yasuda,[48] Y. A. Yatsunenko,[35] Z. Ye,[48] H. Yin,[48] K. Yip,[71] S. W. Youn,[48] J. Yu,[76] S. Zelitch,[79] T. Zhao,[80] B. Zhou,[61] J. Zhu,[61] M. Zielinski,[69] D. Zieminska,[52] and L. Zivkovic[75]

(D0 Collaboration)

[1]*Universidad de Buenos Aires, Buenos Aires, Argentina*
[2]*LAFEX, Centro Brasileiro de Pesquisas Físicas, Rio de Janeiro, Brazil*
[3]*Universidade do Estado do Rio de Janeiro, Rio de Janeiro, Brazil*
[4]*Universidade Federal do ABC, Santo André, Brazil*
[5]*Instituto de Física Teórica, Universidade Estadual Paulista, São Paulo, Brazil*
[6]*Simon Fraser University, Vancouver, British Columbia, and York University, Toronto, Ontario, Canada*
[7]*University of Science and Technology of China, Hefei, People's Republic of China*
[8]*Universidad de los Andes, Bogotá, Colombia*
[9]*Charles University, Faculty of Mathematics and Physics, Center for Particle Physics, Prague, Czech Republic*
[10]*Czech Technical University in Prague, Prague, Czech Republic*
[11]*Center for Particle Physics, Institute of Physics, Academy of Sciences of the Czech Republic, Prague, Czech Republic*
[12]*Universidad San Francisco de Quito, Quito, Ecuador*
[13]*LPC, Université Blaise Pascal, CNRS/IN2P3, Clermont, France*
[14]*LPSC, Université Joseph Fourier Grenoble 1, CNRS/IN2P3, Institut National Polytechnique de Grenoble, Grenoble, France*
[15]*CPPM, Aix-Marseille Université, CNRS/IN2P3, Marseille, France*
[16]*LAL, Université Paris-Sud, CNRS/IN2P3, Orsay, France*
[17]*LPNHE, Universités Paris VI and VII, CNRS/IN2P3, Paris, France*
[18]*CEA, Irfu, SPP, Saclay, France*
[19]*IPHC, Université de Strasbourg, CNRS/IN2P3, Strasbourg, France*
[20]*IPNL, Université Lyon 1, CNRS/IN2P3, Villeurbanne, France and Université de Lyon, Lyon, France*
[21]*III. Physikalisches Institut A, RWTH Aachen University, Aachen, Germany*
[22]*Physikalisches Institut, Universität Freiburg, Freiburg, Germany*
[23]*II. Physikalisches Institut, Georg-August-Universität Göttingen, Göttingen, Germany*
[24]*Institut für Physik, Universität Mainz, Mainz, Germany*
[25]*Ludwig-Maximilians-Universität München, München, Germany*
[26]*Fachbereich Physik, Bergische Universität Wuppertal, Wuppertal, Germany*
[27]*Panjab University, Chandigarh, India*
[28]*Delhi University, Delhi, India*
[29]*Tata Institute of Fundamental Research, Mumbai, India*
[30]*University College Dublin, Dublin, Ireland*
[31]*Korea Detector Laboratory, Korea University, Seoul, Korea*
[32]*CINVESTAV, Mexico City, Mexico*
[33]*Nikhef, Science Park, Amsterdam, The Netherlands*
[34]*Radboud University Nijmegen, Nijmegen, The Netherlands and Nikhef, Science Park, Amsterdam, The Netherlands*
[35]*Joint Institute for Nuclear Research, Dubna, Russia*
[36]*Institute for Theoretical and Experimental Physics, Moscow, Russia*
[37]*Moscow State University, Moscow, Russia*
[38]*Institute for High Energy Physics, Protvino, Russia*
[39]*Petersburg Nuclear Physics Institute, St. Petersburg, Russia*
[40]*Institució Catalana de Recerca i Estudis Avançats and Institut de Física d'Altes Energies, Barcelona, Spain*
[41]*Stockholm University, Stockholm and Uppsala University, Uppsala, Sweden*
[42]*Lancaster University, Lancaster LA1 4YB, United Kingdom*
[43]*Imperial College London, London SW7 2AZ, United Kingdom*
[44]*The University of Manchester, Manchester M13 9PL, United Kingdom*
[45]*University of Arizona, Tucson, Arizona 85721, USA*
[46]*University of California Riverside, Riverside, California 92521, USA*
[47]*Florida State University, Tallahassee, Florida 32306, USA*
[48]*Fermi National Accelerator Laboratory, Batavia, Illinois 60510, USA*
[49]*University of Illinois at Chicago, Chicago, Illinois 60607, USA*
[50]*Northern Illinois University, DeKalb, Illinois 60115, USA*
[51]*Northwestern University, Evanston, Illinois 60208, USA*
[52]*Indiana University, Bloomington, Indiana 47405, USA*

[53]Purdue University Calumet, Hammond, Indiana 46323, USA
[54]University of Notre Dame, Notre Dame, Indiana 46556, USA
[55]Iowa State University, Ames, Iowa 50011, USA
[56]University of Kansas, Lawrence, Kansas 66045, USA
[57]Kansas State University, Manhattan, Kansas 66506, USA
[58]Louisiana Tech University, Ruston, Louisiana 71272, USA
[59]Boston University, Boston, Massachusetts 02215, USA
[60]Northeastern University, Boston, Massachusetts 02115, USA
[61]University of Michigan, Ann Arbor, Michigan 48109, USA
[62]Michigan State University, East Lansing, Michigan 48824, USA
[63]University of Mississippi, University, Mississippi 38677, USA
[64]University of Nebraska, Lincoln, Nebraska 68588, USA
[65]Rutgers University, Piscataway, New Jersey 08855, USA
[66]Princeton University, Princeton, New Jersey 08544, USA
[67]State University of New York, Buffalo, New York 14260, USA
[68]Columbia University, New York, New York 10027, USA
[69]University of Rochester, Rochester, New York 14627, USA
[70]State University of New York, Stony Brook, New York 11794, USA
[71]Brookhaven National Laboratory, Upton, New York 11973, USA
[72]Langston University, Langston, Oklahoma 73050, USA
[73]University of Oklahoma, Norman, Oklahoma 73019, USA
[74]Oklahoma State University, Stillwater, Oklahoma 74078, USA
[75]Brown University, Providence, Rhode Island 02912, USA
[76]University of Texas, Arlington, Texas 76019, USA
[77]Southern Methodist University, Dallas, Texas 75275, USA
[78]Rice University, Houston, Texas 77005, USA
[79]University of Virginia, Charlottesville, Virginia 22901, USA
[80]University of Washington, Seattle, Washington 98195, USA
(Received 13 June 2011; published 14 September 2011)

We present a direct measurement of the mass difference between top and antitop quarks (Δm) in lepton + jets $t\bar{t}$ final states using the ''matrix element'' method. The purity of the lepton + jets sample is enhanced for $t\bar{t}$ events by identifying at least one of the jets as originating from a b quark. The analyzed data correspond to 3.6 fb^{-1} of $p\bar{p}$ collisions at $\sqrt{s} = 1.96$ TeV acquired by D0 in Run II of the Fermilab Tevatron Collider. The combination of the e + jets and μ + jets channels yields $\Delta m = 0.8 \pm 1.8(\text{stat}) \pm 0.5(\text{syst})$ GeV, which is in agreement with the standard model expectation of no mass difference.

DOI: 10.1103/PhysRevD.84.052005 PACS numbers: 14.65.Ha

I. INTRODUCTION

The standard model (SM) is a local gauge-invariant quantum field theory (QFT), with invariance under charge, parity, and time reversal (CPT) providing one of its most fundamental principles [1–4], which also constrains the SM [5]. In fact, any Lorentz-invariant local QFT must conserve CPT [6]. A difference in the mass of a particle and its antiparticle would constitute a violation of CPT invariance. This issue has been tested extensively for many elementary particles of the SM [7]. Quarks, however, carry color charge, and therefore are not observed directly, but must first hadronize via QCD processes into jets of colorless particles. These hadronization products reflect properties of the initially produced quarks, such as their masses, electric charges, and spin states. Except for the top quark, the time scale for hadronization of quarks is orders of magnitude less than for electroweak decay, thereby favoring the formation of QCD-bound hadronic states before decay. This introduces a significant dependence of the mass of a quark on the model of QCD binding and evolution. In contrast to other quarks, no bound states are formed before the decay of the produced top quarks, thereby providing a unique opportunity to measure directly the mass difference between a quark and its antiquark [8].

In proton-antiproton collisions at the Fermilab Tevatron Collider, top quarks are produced in $t\bar{t}$ pairs via the strong interaction, or singly via the electroweak interaction. In the SM, the top quark decays almost exclusively into a W boson and a b quark. The topology of a $t\bar{t}$ event is therefore

*Visitor from Augustana College, Sioux Falls, SD, USA.
†Visitor from The University of Liverpool, Liverpool, UK.
‡Visitor from SLAC, Menlo Park, CA, USA.
§Visitor from University College London, London, UK.
‖Visitor from Centro de Investigacion en Computacion–IPN, Mexico City, Mexico.
¶Visitor from ECFM, Universidad Autonoma de Sinaloa, Culiacán, Mexico.
**Visitor from Universität Bern, Bern, Switzerland.
††Deceased.

determined by the subsequent decays of the W bosons. The world's most precise top quark mass measurements are performed in the lepton + jets (ℓ + jets) channels, which are characterized by the presence of one isolated energetic electron or muon from one $W \to \ell\nu$ decay, an imbalance in transverse momentum relative to the beam axis from the escaping neutrino, and four or more jets from the evolution of the two b quarks and the two quarks from the second $W \to q\bar{q}'$ decay.

The top quark was discovered [9,10] in proton-antiproton collision data at a center-of-mass energy of $\sqrt{s} = 1.8$ TeV in Run I of the Tevatron. After an upgrade to a higher center-of-mass energy of $\sqrt{s} = 1.96$ TeV and higher luminosities, Run II of the Tevatron commenced in 2001. Since then, a large sample of $t\bar{t}$ events has been collected, yielding precision measurements of various SM parameters such as the mass of the top quark, which has been determined to an accuracy of about 0.6% or $m_{\text{top}} \equiv \frac{1}{2}(m_t + m_{\bar{t}}) = 173.3 \pm 1.1$ GeV [11], where m_t ($m_{\bar{t}}$) is the mass of the top (antitop) quark.

The D0 Collaboration published the first measurement of the top-antitop quark mass difference, $\Delta m \equiv m_t - m_{\bar{t}}$, using 1 fb^{-1} of Run II integrated luminosity [12]. Our new measurement, presented here, employs the same matrix element (ME) technique [13,14], suggested initially by Kondo *et al.* [15–17], and developed to its current form by D0 [18]. Our previous study measured a mass difference

$$\Delta m = 3.8 \pm 3.4(\text{stat}) \pm 1.2(\text{syst}) \text{ GeV}.$$

Recently, CDF has also measured Δm [19] based on 5.6 fb^{-1} of Run II data, using a template technique, and found

$$\Delta m = -3.3 \pm 1.4(\text{stat}) \pm 1.0(\text{syst}) \text{ GeV}.$$

In this paper, we extend our first measurement of Δm using an additional 2.6 fb^{-1} of Run II integrated luminosity, and combining our two results. We also reexamine the uncertainties from the modeling of signal processes and of the response of the detector. Most important is a possible presence of asymmetries in the calorimeter response to b- and $\bar{b}$-quark jets, which we reevaluate using a purely data-driven method. We also consider for the first time a bias from asymmetries in response to c- and $\bar{c}$-quark jets.

This paper is arranged as follows: after a brief description of the D0 detector in Sec. II, we review the event selection and reconstruction in Sec. III. In Sec. IV, we define the samples of Monte Carlo (MC) events used in the analysis. The extraction of the top-antitop quark mass difference using the ME technique is then briefly reviewed in Sec. V. The calibration of this technique, based on MC events, and the measurement of the mass difference in 2.6 fb^{-1} of Run II integrated luminosity are presented in Sec. VI. The evaluation of systematic uncertainties and cross-checks are discussed in Sec. VII and VII C, respectively. Finally, the combination of the measurements for the 2.6 fb^{-1} and 1 fb^{-1} data samples is presented in Sec. VIII.

II. THE D0 DETECTOR

The D0 detector has a central-tracking system, calorimetry, and a muon system. The central-tracking system consists of a silicon microstrip tracker (SMT) and a central fiber tracker (CFT), both located within a 1.9 T superconducting solenoidal magnet [20–22], with designs optimized for tracking and vertexing at pseudorapidities $|\eta| < 3$ [23]. The SMT can reconstruct the $p\bar{p}$ interaction vertex (PV) with a precision of about 40 μm in the plane transverse to the beam direction and determine the impact parameter of any track relative to the PV [24] with a precision between 20 and 50 μm, depending on the number of hits in the SMT. These are the key elements to lifetime-based b-quark jet tagging. The liquid-argon and uranium sampling calorimeter has a central section (CC) covering pseudorapidities $|\eta| \lesssim 1.1$ and two end calorimeters (EC) that extend coverage to $|\eta| \approx 4.2$, with all three housed in separate cryostats [20,25]. Central and forward preshower detectors are positioned just before the CC and EC. An outer muon system, at $|\eta| < 2$, consists of a layer of tracking detectors and scintillation trigger counters in front of 1.8 T toroids, followed by two similar layers after the toroids [26]. The luminosity is calculated from the rate of $p\bar{p}$ inelastic collisions measured with plastic scintillator arrays, which are located in front of the EC cryostats. The trigger and data acquisition systems are designed to accommodate the high instantaneous luminosities of Run II [27].

III. EVENT SELECTION

In this new measurement of Δm, we analyze data corresponding to an integrated luminosity of about 2.6 fb^{-1} for both the e + jets and μ + jets channels.

Candidate $t\bar{t}$ events are required to pass an isolated energetic lepton trigger or a lepton + jet(s) trigger. These events are enriched in $t\bar{t}$ content by requiring exactly four jets reconstructed using the Run II cone algorithm [28] with cone radius $\Delta R \equiv \sqrt{(\Delta\eta)^2 + (\Delta\phi)^2} = 0.5$, transverse momenta $p_T > 20$ GeV, and pseudorapidities $|\eta| < 2.5$. The jet of highest transverse momentum in a given event must have $p_T > 40$ GeV. Furthermore, we require exactly one isolated electron with $p_T > 20$ GeV and $|\eta| < 1.1$, or exactly one isolated muon with $p_T > 20$ GeV and $|\eta| < 2.0$. The leptons must originate within 1 cm of the PV in the coordinate along the beam line. Events containing an additional isolated lepton (either e or μ) with $p_T > 15$ GeV are rejected. Lepton isolation criteria are based on calorimetric and tracking information along with object identification criteria, as described in Ref. [29]. The positively (negatively) charged leptons are used to tag the top (antitop) quark in a given event. To reduce instrumental

TABLE I. A summary of kinematic event selections applied.

Exactly one charged lepton	$p_T > 20$ GeV	$\|\eta\| < 1.1$ (e)
	$p_T > 20$ GeV	$\|\eta\| < 2.0$ (μ)
Exactly four jets	$p_T > 20$ GeV	$\|\eta\| < 2.5$
Jet of highest p_T	$p_T > 40$ GeV	$\|\eta\| < 2.5$
Imbalance in transverse momentum	$\not{p}_T > 20$ GeV	(e + jets)
	$\not{p}_T > 25$ GeV	(μ + jets)

effects that can cause charge-dependent asymmetries in the lepton momentum scale, the polarity of the solenoidal magnetic field is routinely reversed, splitting the total data into two samples of approximately equal size. The PV must have at least three associated tracks and lie within the fiducial region of the SMT. At least one neutrino is expected in the ℓ + jets final state; hence, an imbalance in transverse momentum (defined as the opposite of the vector sum of the transverse energies in each calorimeter cell, corrected for the energy carried by identified muons and energy added or subtracted due to the jet energy scale calibration described below) of $\not{p}_T > 20$ GeV (25 GeV) must be present in the e + jets (μ + jets) channel. These kinematic selections are summarized in Table I.

To reduce the contribution of multijet production (MJ) in the e + jets channel, $\Delta\phi(e, \not{p}_T) > 2.2 - \not{p}_T \times 0.045\,\mathrm{GeV}^{-1}$ is required for the azimuthal difference $\Delta\phi(e, \not{p}_T) = |\phi_e - \phi_{\not{p}_T}|$ between the electron and the direction of $\not{p}_T$. Likewise, $\Delta\phi(\mu, \not{p}_T) > 2.1 - \not{p}_T \times 0.035\ \mathrm{GeV}^{-1}$ is required in the μ + jets channel. Jets from b quarks are identified by a neural-network-based b-tagging algorithm [30], which combines variables that characterize properties of secondary vertices and tracks within the jet that have large impact parameters relative to the PV. Typically, its efficiency for b-quark jets is about 65%, while the probability for misidentifying u-, d-, s-quark and gluon jets as b jets is about 3%. To increase $t\bar{t}$ purity, and to reduce the number of combinatoric possibilities for assigning jets to $t\bar{t}$ decay products, we require at least one b-tagged jet to be present in the events used to measure Δm.

After all acceptance requirements, a data sample of 312 (303) events is selected in the e + jets (μ + jets) channel. As discussed above, each of those samples is split according to lepton charge. In the e + jets channel, 174 (138) events have a positive (negative) lepton in the final state. Likewise, the μ + jets sample is split into subsets of 145 and 158 events.

IV. MONTE CARLO SIMULATION

Large samples of simulated MC events are used to determine the resolution of the detector and to calibrate the Δm measurement as well as the statistical sensitivity of the method. After simulation of the hard-scattering part of the interaction and parton shower corrections, MC events are passed through a detailed detector simulation based on GEANT [31], overlaid with data collected from a random subsample of beam crossings to model the effects of noise and multiple interactions, and reconstructed using the same algorithms that are used for data. Although the fraction of signal events, f, is fitted in the analysis, we also cross-check that the entire data sample is described adequately by the simulations.

A. Monte Carlo samples for signal

Simulated $t\bar{t}$ events with different m_t and $m_{\bar{t}}$ are required to calibrate the Δm measurement. We use the PYTHIA generator [32], version 6.413, to model the $t\bar{t}$ signal. This generator models the Breit-Wigner shape of the invariant mass distribution of t and $\bar{t}$ quarks, whose correct description is important for the Δm measurement.

In the standard PYTHIA, it is not possible to generate $t\bar{t}$ events with different masses m_t and $m_{\bar{t}}$. Therefore, we modify the PYTHIA program to provide signal events with $m_t \neq m_{\bar{t}}$. In applying these modifications, we adjust the description of all quantities that depend on the two masses, for example, the respective decay widths Γ_t and $\Gamma_{\bar{t}}$. Technical details of this implementation can be found in the Appendix.

We generate $t\bar{t}$ events using the CTEQ6L1 parton distribution function set (PDF) [33] at the momentum transfer scale $Q^2 = (p_T^{\mathrm{scat}})^2 + \frac{1}{2}\{P_1^2 + P_2^2 + m_t^2 + m_{\bar{t}}^2\}$, where p_T^{scat} is the transverse momentum for the hard-scattering process, and P_i is the four-momentum of the incoming parton i. For $m_t = m_{\bar{t}}$, the expression used for Q^2 is identical to that in the standard PYTHIA. All other steps in the event simulation process, aside from the generation of the hard-scattering process, e.g., the modeling of the detector response, are unchanged from the standard PYTHIA.

We check our modified PYTHIA version against the original by comparing large samples of simulated $t\bar{t}$ events for $(m_t, m_{\bar{t}}) = (170\ \mathrm{GeV}, 170\ \mathrm{GeV})$, at both the parton and reconstruction levels, and find full consistency.

The $t\bar{t}$ samples are generated at 14 combinations of top and antitop quark masses $(m_t, m_{\bar{t}})$, which form a grid spaced at 5 GeV intervals between (165 GeV, 165 GeV) and (180 GeV, 180 GeV), excluding the two extreme points at (165 GeV, 180 GeV) and (180 GeV, 165 GeV). The four points with $m_t = m_{\bar{t}}$ are generated with the standard PYTHIA, whereas all others use our modified version of the generator.

B. Monte Carlo and other simulations of background

The dominant background to $t\bar{t}$ decays into ℓ + jets final states is from the electroweak production of a W boson in association with jets from gluon radiation. We simulate the hard-scattering part of this process using the ALPGEN MC program [34], which is capable of simulating up to five additional particles in the final state at LO in α_s. ALPGEN is coupled to PYTHIA, which is used to model the hadronization of the partons and the evolution of the shower. The Michelangelo L. Mangano (or MLM) matching scheme is applied to avoid double-counting of partonic event configurations [35]. The W + jets contribution is divided into two categories according to parton flavor: (i) $W + b\bar{b}$ + jets and $W + c\bar{c}$ + jets and (ii) all other contributions, where ''jets'' generically denotes jets from u, d, s quarks and gluons. The second category also includes the $W + c$ + jets final states. While the individual processes are generated with ALPGEN, the relative contributions of the two categories are determined using next-to-LO (NLO) calculations, with next-to-leading logarithmic (NLL) corrections based on the MCFM MC generator [36]. These NLO corrections increase the LO cross section of category (i) by a factor of $k = 1.47 \pm 0.22$, while $k = 1$ is used for category (ii). The resulting combined W + jets background contribution is then determined from a fit to data and predictions for other signal and background contributions, as described in Sec. V. Thus, the NLO k factors only change the relative balance between (i) and (ii).

Additional background contributions arise from WW, WZ, ZZ, single top quark electroweak production, $Z \to \tau\tau$, and $Z \to ee$ ($Z \to \mu\mu$) production in the e + jets (μ + jets) channel. The predictions for these backgrounds are taken from MC simulations, and, with the exception of single top quark electroweak production, their production cross sections are normalized to NLO + NLL calculations with MCFM. Diboson processes are simulated with PYTHIA. The hard-scattering part of single top quark production is simulated with COMPHEP [37], while ALPGEN is used for Z + jets boson production. For both backgrounds, PYTHIA is employed to model hadronization and shower evolution. The CTEQ6L1 PDFs and the D0 tune A underlying event model [38] are used in the generation of all MC samples.

Events from MJ production can pass our selection criteria, which typically happens when a jet mimics an electron, or a muon that arises from a semileptonic decay of a b or c quark appears to be isolated. The kinematic distributions of the MJ background are modeled using events in data that fail only the electron identification (muon isolation) criteria, but pass loosened versions of these criteria defined in [40]. The absolute contribution of this background to each of the channels is estimated using the method described in Ref. [40]. This method uses the absolute numbers of events with prompt leptons $N_{\text{loose}}^{t\bar{t}+W}$ and events from MJ production $N_{\text{loose}}^{\text{MJ}}$ in the sample with loosened lepton identification criteria, and relates them to the absolute contributions to the sample with standard lepton identification criteria via $N = \varepsilon^{t\bar{t}+W} N_{\text{loose}}^{t\bar{t}+W} + \varepsilon^{\text{MJ}} N_{\text{loose}}^{\text{MJ}}$. Here, $\varepsilon^{t\bar{t}+W}$ and ε^{MJ} represent the efficiency of events which pass the loosened lepton identification criteria to also pass the standard identification criteria, and are measured in control regions dominated by prompt leptons and MJ events, respectively.

C. Event yields

We split the selected ℓ + jets events into subsamples according to lepton flavor (e or μ), jet multiplicity, and the number of b-tagged jets in the event to verify an adequate description of the data with our signal and background model. In general, we observe good agreement between data and simulations, and systematic uncertainties on the final result explicitly account for moderate agreement observed in some kinematic distributions (cf. Sec. VII).

The numbers of events surviving the final stage of selection with at least one b tag are summarized in Table II. Here, for ease of comparison, the contributions from $t\bar{t}$ events are scaled to $7.45^{+0.5}_{-0.7}$ pb, the NLO cross section including next-to-NLO approximations [41]. The total W + jets cross section is adjusted to bring the absolute yield from our signal and background model into agreement with the number of events selected in data before applying b-jet identification criteria. The distributions in the transverse mass of the W boson, M_T^W [42], and in $\not\!\!p_T$ are shown in Fig. 1 for data with at least one b tag, together with the predictions from our signal and background models.

TABLE II. Numbers of events selected in data, compared to yield predictions for individual processes using simulations, in the e + jets and μ + jets channels with exactly four jets and at least one b-tagged jet, split according to b-tag multiplicity. Uncertainties are purely statistical. See text for details.

	$1b$ tag	$>1b$ tags
e + jets		
$t\bar{t}$	139.2 ± 3.0	91.8 ± 2.5
W + jets	39.9 ± 1.2	4.7 ± 0.3
MJ	23.5 ± 2.1	5.7 ± 1.0
Z + jets	7.6 ± 0.7	0.9 ± 0.1
Other	6.6 ± 0.4	1.9 ± 0.1
Total	216.7 ± 3.9	105.1 ± 2.7
Observed	223	89
μ + jets		
$t\bar{t}$	105.9 ± 2.4	70.9 ± 2.0
W + jets	59.9 ± 1.8	7.2 ± 0.5
MJ	5.2 ± 0.9	2.0 ± 0.6
Z + jets	5.3 ± 0.5	1.2 ± 0.2
Other	5.0 ± 0.3	1.3 ± 0.1
Total	181.3 ± 3.2	82.6 ± 2.2
Observed	191	112

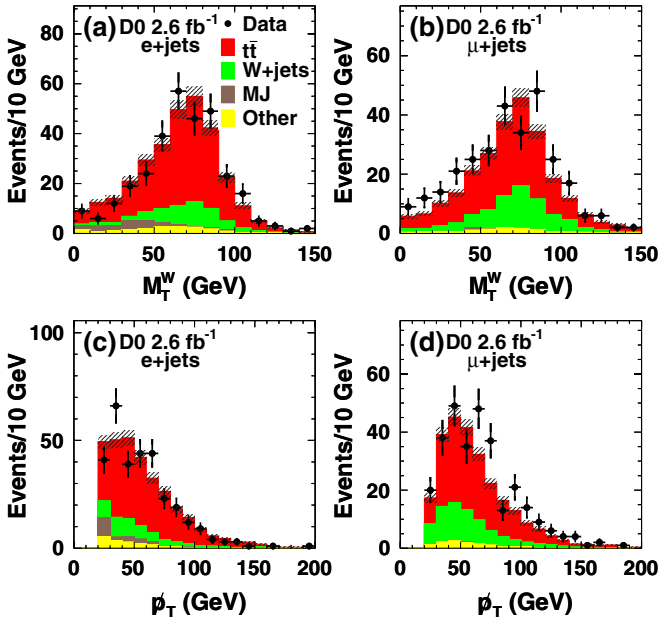

FIG. 1 (color online). The transverse mass of the W boson M_T^W for events with at least one b tag is shown for the (a) e + jets and (b) μ + jets channels. Similarly, $\not{p}_T$ is shown for the (c) e + jets and (d) μ + jets channels. The statistical uncertainties on the prediction from the $t\bar{t}$ signal and background models are indicated by the hatched area.

V. GENERAL DESCRIPTION OF THE METHOD

In this section, we describe the measurement of Δm using the ME method. The procedure is similar to the one used in Refs. [13,43] to measure the average top quark mass m_{top}, but instead of simultaneously determining m_{top} and the jet energy scale (JES), here we measure directly the masses of the top and antitop quarks, m_t and $m_{\bar{t}}$, which provides Δm and m_{top}. We review the ME approach in Sec. V A and the calculation of signal and background event probabilities in Secs. V B and V C, respectively, as well as the parametrization of the detector response and the use of b-tagging information in Sec. V D.

A. Probability densities for events

To optimize the use of kinematic and topological information, each event is assigned a probability P_{evt} to observe it as a function of the assumed top and antitop quark masses: $P_{\text{evt}} = P_{\text{evt}}(m_t, m_{\bar{t}})$. The individual probabilities for all events in a given sample are combined to form a likelihood, from which the Δm and m_{top} parameters are extracted. Simplifying assumptions are made in the expression of the likelihood about, e.g., detector response or the sample composition, to render the problem numerically solvable. It is therefore necessary to calibrate the method using fully simulated MC events, as detailed in Sec. VI B. Systematic uncertainties are estimated to account for possible effects of these assumptions on the extracted value of Δm.

Assuming that the signal and background physics processes do not interfere, the contribution to the overall probability from a single event can be formulated as

$$P_{\text{evt}}(x; m_t, m_{\bar{t}}, f) = A(x)\{f \cdot P_{\text{sig}}(x; m_t, m_{\bar{t}}) + (1 - f) \cdot P_{\text{bkg}}(x)\}, \quad (1)$$

where x denotes the set of measured kinematic variables for the event observed in the detector, f is the fraction of signal events in the sample, $A(x)$ reflects the detector acceptance and efficiencies for a given x, and P_{sig} and P_{bkg} are the probabilities for the event to arise from $t\bar{t}$ or W + jets production, respectively. The production of W bosons in association with jets is the dominant background, and we neglect all other contributions to P_{bkg}. Kinematically similar contributions from other background processes like MJ production are accounted for in the analysis implicitly (cf. Sec. VII).

Both signal and background probabilities depend on the JES, which is defined as the ratio of the calibrated energy of a jet over its uncalibrated energy. The standard calibration of jet energies accounts for the energy response of the calorimeters, the energy that crosses the cone boundary due to the transverse shower size, and the additional energy from pileup of events and from multiple $p\bar{p}$ interactions in a single beam crossing. Although the Δm observable is not expected to show a strong dependence on JES by construction, we apply an additional absolute calibration to the JES using a matrix element which is a function of m_{top} and JES from Refs. [13,43]. The potential systematic bias on Δm from the uncertainty on the absolute value of the JES is estimated in Sec. VII.

To extract the masses m_t and $m_{\bar{t}}$ from a set of n selected events, with sets of measured kinematic quantities $x_1, \ldots, x_n$, a likelihood function is defined from the individual event probabilities according to Eq. (1):

$$L(x_1, \ldots, x_n; m_t, m_{\bar{t}}, f) = \prod_{i=1}^{n} P_{\text{evt}}(x_i; m_t, m_{\bar{t}}, f). \quad (2)$$

For every assumed $(m_t, m_{\bar{t}})$ pair, we first determine the value of $f \equiv f^{\text{best}}$ that maximizes this likelihood.

B. Calculation of signal probability P_{sig}

The probability density for the signal to yield a given set of partonic final-state four-momenta y in $p\bar{p}$ collisions is proportional to the differential cross section $d\sigma$ for $t\bar{t}$ production:

$$d\sigma(p\bar{p} \to t\bar{t} \to y; m_t, m_{\bar{t}}) = \int_{q_1,q_2} \sum_{\text{quark flavors}} dq_1 dq_2 f(q_1) f(q_2) \times \frac{(2\pi)^4 |\mathcal{M}(q\bar{q} \to t\bar{t} \to y)|^2}{2q_1 q_2 s} d\Phi_6, \quad (3)$$

where $\mathcal{M}$ denotes the matrix element for the $q\bar{q} \to t\bar{t} \to b(l\nu)\bar{b}(q\bar{q}')$ process, s is the square of the center-of-mass energy, q_i is the momentum fraction of the colliding parton i (assumed to be massless), and $d\Phi_6$ is an infinitesimal element of six-body phase space. The $f(q_i)$ denote the probability densities for finding a parton of given flavor and momentum fraction q_i in the proton or antiproton, and the sum runs over all possible flavor configurations of the colliding quark and antiquark. In our definition of $\mathcal{M}$, and therefore the $t\bar{t}$ signal probability, only quark-antiquark annihilation at LO is taken into account; in this sense, Eq. (3) does not represent the full differential cross section for $t\bar{t}$ production in $p\bar{p}$ collisions. Effects from gluon-gluon and quark-gluon induced $t\bar{t}$ production are accounted for in the calibration procedure described in Sec. VI B. We further test for an effect on Δm from higher-order corrections in Sec. VII C.

The differential cross section for observing a $t\bar{t}$ event with a set of kinematic quantities x measured in the detector can be written as

$$d\sigma(p\bar{p} \to t\bar{t} \to x; m_t, m_{\bar{t}}, k_{\mathrm{JES}}) = A(x) \int_y dy d\sigma(p\bar{p} \to t\bar{t} \to y; m_t, m_{\bar{t}}) W(x, y; k_{\mathrm{JES}}), \quad (4)$$

where finite detector resolution and offline selections are taken explicitly into account through the convolution over a transfer function $W(x, y; k_{\mathrm{JES}})$ that defines the probability for a partonic final state y to appear as x in the detector given an absolute JES correction k_{JES}.

With the above definitions, the differential probability to observe a $t\bar{t}$ event with a set of kinematic quantities x measured in the detector is given by

$$P_{\mathrm{sig}}(x; m_t, m_{\bar{t}}, k_{\mathrm{JES}}) = \frac{d\sigma(p\bar{p} \to t\bar{t} \to x; m_t, m_{\bar{t}}, k_{\mathrm{JES}})}{\sigma_{\mathrm{obs}}(p\bar{p} \to t\bar{t}; m_t, m_{\bar{t}}, k_{\mathrm{JES}})}, \quad (5)$$

where σ_{obs} is the cross section for observing $t\bar{t}$ events in the detector for the specific ME $\mathcal{M}$ defined in Eq. (3):

$$\begin{aligned}\sigma_{\mathrm{obs}}(p\bar{p} \to t\bar{t}; m_t, m_{\bar{t}}, k_{\mathrm{JES}}) &= \int_{x,y} dx dy d\sigma(p\bar{p} \to t\bar{t} \to y; m_t, m_{\bar{t}}) W(x, y; k_{\mathrm{JES}}) A(x) \\ &= \int_y dy d\sigma(p\bar{p} \to t\bar{t} \to y; m_t, m_{\bar{t}}) \int_x dx W(x, y; k_{\mathrm{JES}}) A(x).\end{aligned}$$

The normalization factor σ_{obs} is calculated using MC integration techniques:

$$\sigma_{\mathrm{obs}}(p\bar{p} \to t\bar{t}; m_t, m_{\bar{t}}, k_{\mathrm{JES}}) \simeq \sigma_{\mathrm{tot}}(m_t, m_{\bar{t}}) \langle A | m_t, m_{\bar{t}} \rangle, \quad (6)$$

where

$$\sigma_{\mathrm{tot}}(m_t, m_{\bar{t}}) = \int_y dy d\sigma(p\bar{p} \to t\bar{t} \to y; m_t, m_{\bar{t}}) \quad (7)$$

and

$$\langle A | m_t, m_{\bar{t}} \rangle \equiv \frac{1}{N_{\mathrm{gen}}} \sum_{\mathrm{acc}} \omega. \quad (8)$$

To calculate the $\langle A | m_t, m_{\bar{t}} \rangle$ term, events are generated according to $d\sigma(p\bar{p} \to t\bar{t}; m_t, m_{\bar{t}})$ using PYTHIA and passed through the full simulation of the detector. Here, N_{gen} is the total number of generated events, ω are the MC event weights that account for trigger and identification efficiencies, and the sum runs over all accepted events.

The formulas used to calculate the total cross section σ_{tot} and the matrix element $\mathcal{M}$ are described below in Secs. V B 1 and V B 2. In all other respects, the calculation of the signal probability proceeds identically to that in Refs. [13,43], with the following exceptions: (i) CTEQ6L1 PDFs are used throughout, and (ii) the event probabilities are calculated on a grid in m_t and $m_{\bar{t}}$ spaced at 1 GeV intervals along each axis. As described in Sec. VI A, a transformation of variables to Δm and m_{top} is performed when defining the likelihood.

1. Calculation of the total cross section σ_{tot}

Without the assumption of equal top and antitop quark masses, the total LO cross section for the $q\bar{q} \to t\bar{t}$ process in the center-of-mass frame is given by

$$\sigma = \frac{16\pi\alpha_s^2}{27 s^{5/2}} |\vec{p}| [3E_t E_{\bar{t}} + |\vec{p}|^2 + 3m_t m_{\bar{t}}], \quad (9)$$

where E_t ($E_{\bar{t}}$) are the energies of the top and antitop quark, and $\vec{p}$ is the three-momentum of the top quark. This reduces to the familiar form for $m_t = m_{\bar{t}}$:

$$\sigma = \frac{4\pi\alpha_s^2}{9s} \beta \left(1 - \frac{\beta^2}{3}\right),$$

where $\beta = |\vec{p}_t|/E_t = |\vec{p}_{\bar{t}}|/E_{\bar{t}}$ represents the velocity of the t (or $\bar{t}$) quark in the $q\bar{q}$ rest frame.

Integrating Eq. (9) over all incoming $q\bar{q}$ momenta and using the appropriate PDF yields $\sigma_{\mathrm{tot}}(p\bar{p} \to t\bar{t}; m_t, m_{\bar{t}})$, as defined for any values of m_t and $m_{\bar{t}}$ in Eq. (7). Figure 2 displays the dependence of σ_{tot} on Δm for a given m_{top}. The corresponding average acceptance term $\langle A | m_t, m_{\bar{t}} \rangle$, as defined in the same equation, is shown in Fig. 3 for the e + jets and μ + jets channels.

2. Calculation of the matrix element $\mathcal{M}$

The LO matrix element for the $q\bar{q} \to t\bar{t}$ process we use in our analysis is

$$|\mathcal{M}|^2 = \frac{g_s^4}{9} F\bar{F} \cdot \frac{2}{s} \{(E_t - |\vec{p}_t| c_{qt})^2 + (E_{\bar{t}} + |\vec{p}_{\bar{t}}| c_{qt})^2 + 2m_t m_{\bar{t}}\}. \quad (10)$$

The form factors $F\bar{F}$ are identical to those given in Eqs. (24) and (25) of Ref. [13]. For the special case of $m_t = m_{\bar{t}}$, the expression in Eq. (10) reduces to

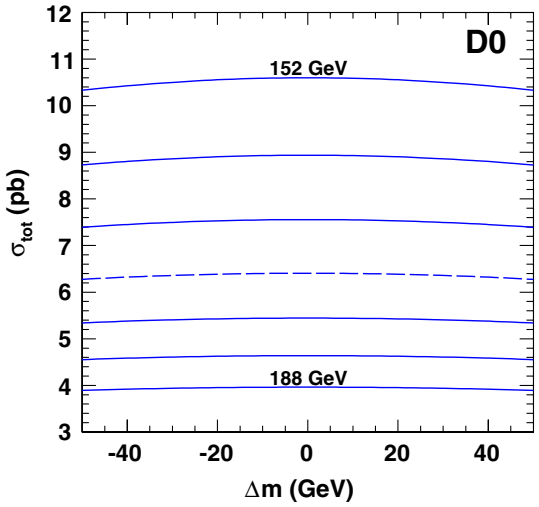

FIG. 2 (color online). The total $p\bar{p} \to t\bar{t}$ production cross section $\sigma_{\rm tot}$ defined in Eq. (7) as a function of Δm and $m_{\rm top}$. Each line shows $\sigma_{\rm tot}$ as a function of Δm for a given value of $m_{\rm top}$ displayed above the curve. The range from 152 GeV to 188 GeV is shown in 6 GeV increments; the broken line corresponds to 170 GeV.

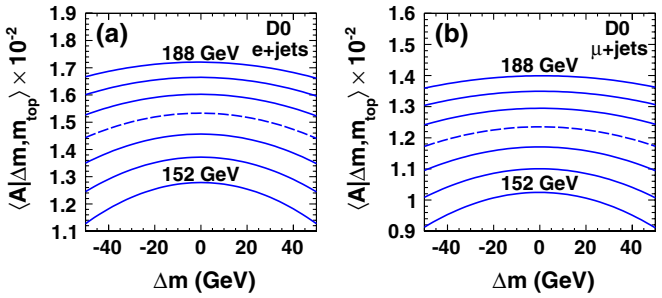

FIG. 3 (color online). The dependence of the overall average acceptance $\langle A|m_t, m_{\bar{t}}\rangle$ on Δm and $m_{\rm top}$, as defined in Eq. (6), for the (a) e + jets and (b) μ + jets signal MC samples. Each line shows $\langle A|m_t, m_{\bar{t}}\rangle$ as a function of Δm for a given value of $m_{\rm top}$ displayed above the curve. The range from 152 GeV to 188 GeV is shown in 6 GeV increments; the broken lines correspond to 170 GeV.

$$|\mathcal{M}|^2 = \frac{g_s^4}{9} F\bar{F} \cdot (2 - \beta^2 s_{qt}^2),$$

which is identical to Refs. [13,44], where s_{qt} is the sine of the angle between the incoming parton and the outgoing top quark in the $q\bar{q}$ rest frame.

C. Calculation of the background probability $P_{\rm bkg}$

The expression for the background probability $P_{\rm bkg}$ is similar to that for $P_{\rm sig}$ in Eq. (5), except that the ME $\mathcal{M}_{W+\rm jets}$ is for W + jets production, and all jets are assumed to be light quark or gluon jets. Clearly, $\mathcal{M}_{W+\rm jets}$ does not depend on m_t or $m_{\bar{t}}$, and $P_{\rm bkg}$ is therefore independent of either. We use a LO parametrization of $\mathcal{M}$ from the VECBOS [45] program. More details on the calculation of the background probability can be found in Ref. [13].

D. Description of detector response

The transfer function $W(x, y, k_{\rm JES})$, which relates the set of variables x characterizing the reconstructed final-state objects to their partonic quantities y, is crucial for the calculation of the signal probability according to Eq. (5), and the corresponding expression for $P_{\rm bkg}$. A full simulation of the detector would not be feasible for calculating event probabilities because of the overwhelming requirements for computing resources. Therefore, we parametrize the detector response and resolution through a transfer function.

In constructing the transfer function, we assume that the functions for individual final-state particles are not correlated. We therefore factorize the transfer function into contributions from each measured final-state object used in calculating $P_{\rm sig}$, that is, the isolated lepton and four jets. The poorly measured imbalance in transverse momentum $\not{p}_T$, and consequently the transverse momentum of the neutrino, is not used in defining event probabilities. We assume that the directions of e, μ, and jets in (η, ϕ) space are well measured, and therefore define the transfer functions for these quantities as δ functions: $\delta^2(\eta, \phi) \equiv \delta(\eta_y - \eta_x)\delta(\phi_y - \phi_x)$. This reduces the number of integrations over the six-particle phase space $d\Phi_6$ by $5 \times 2 = 10$ dimensions. The magnitudes of particle momenta $|\vec{p}|$ display significant variations in resolution for leptons and jets and are therefore parametrized by their corresponding resolutions.

There is an inherent ambiguity in assigning jets reconstructed in the detector to specific partons from $t\bar{t}$ decay. Consequently, all 24 permutations of jet-quark assignments are considered in the analysis. The inclusion of b-tagging information provides improved identification of the correct permutation. This additional information enters the probability calculation through a weight w_i on a given permutation i of jet-parton assignments. The w_i are larger for those permutations that assign the b-tagged jets to b quarks and untagged jets to light quarks. The sum of weights is normalized to unity: $\sum_{i=1}^{24} w_i = 1$.

Based on the above, we define the transfer function as

$$W(x, y; k_{\rm JES}) = W_\ell(E_x, E_y)\delta_\ell^2(\eta, \phi) \times \sum_{i=1}^{24} w_i \left\{ \prod_{j=1}^{4} \delta_{ij}^2(\eta, \phi) W_{\rm jet}(E_x^i, E_y^j; k_{\rm JES}) \right\}, \quad (11)$$

where ℓ denotes the lepton flavor, with a term W_e describing the energy resolution for electrons and W_μ the resolution in the transverse momentum for muons. Similarly, $W_{\rm jet}$ describes the energy resolution for jets. The sum in i is

taken over the 24 possible permutations of assigning jets to quarks in a given event. More details on W_ℓ and $W_{\rm jet}$ can be found in Ref. [43].

The weight w_i for a given permutation i is defined by a product of individual weights w_i^j for each jet j. For b-tagged jets, w_i^j is equal to the per-jet tagging efficiency $\epsilon_{\rm tag}(\alpha_k; E_T^j, \eta^j)$, where α_k labels the three possible parton-flavor assignments of the jet: (i) b quark, (ii) c quark, and (iii) light (u, d, s) quark or gluon. For untagged jets, the w_i^j factors are equal to $1 - \epsilon_{\rm tag}(\alpha_k; E_T^j, \eta^j)$.

Because the contributions to W + jets are parametrized by $\mathcal{M}_{W+\rm jets}$ without regard to heavy-flavor content, the weights w_i for each permutation in the background probability are all set equal.

VI. MEASUREMENT OF THE TOP-ANTITOP QUARK MASS DIFFERENCE

A. Fit to the top-antitop quark mass difference

For the set of selected events, the likelihood $L(m_t, m_{\bar{t}})$ is calculated from Eq. (2) (Sec. V A). The signal fraction $f^{\rm best}$ that maximizes the likelihood is determined at each $(m_t, m_{\bar{t}})$ point for grid spacings of 1 GeV. Subsequently, a transformation is made to the more appropriate set of variables $(\Delta m, m_{\rm top})$:

$$L(x_1, \ldots, x_n; \Delta m, m_{\rm top}) = L[x_1, \ldots, x_n; \Delta m, m_{\rm top}, f^{\rm best}(\Delta m, m_{\rm top})]. \quad (12)$$

To obtain the best estimate of Δm in data, the two-dimensional likelihood in Eq. (12) is projected onto the Δm axis, and the mean value $\langle \Delta m \rangle$ that maximizes it as well as the uncertainty $\delta_{\Delta m}$ on $\langle \Delta m \rangle$ are calculated. This procedure accounts for any correlations between Δm and $m_{\rm top}$. As a consistency check, we simultaneously extract the average mass $m_{\rm top}$ by exchanging $\Delta m \leftrightarrow m_{\rm top}$ above.

B. Calibration of the method

We calibrate the ME method by performing 1000 MC pseudoexperiments at each input point $(m_t, m_{\bar{t}})$. These are used to correlate the fitted parameters with their true input values and to assure the correctness of the estimated uncertainties. Each pseudoexperiment is formed by drawing $N_{\rm sig}$ signal and $N_{\rm bkg}$ background events from a large pool of fully simulated $t\bar{t}$ and W + jets MC events. We assume that W + jets events also represent the kinematic distributions expected from MJ production and other background processes with smaller contributions, and evaluate a systematic uncertainty from this assumption. Events are drawn randomly and can be used more than once, and an "oversampling" correction [46] is applied. The size of each pseudoexperiment, $N = N_{\rm sig} + N_{\rm bkg}$, is fixed by the total number of events observed in the data, i.e., $N = 312$ (303) events for the e + jets (μ + jets) channel. The fraction of signal events is allowed to fluctuate relative to the signal fraction f determined from data (Sec. VI B 1), assuming binomial statistics. The same W + jets background sample is used to form pseudoexperiments for each $(m_t, m_{\bar{t}})$ mass point.

1. Determining the signal fraction in data

The signal fraction f is determined independently for the e + jets and μ + jets channels directly from the selected data sample. The likelihood depends explicitly on three parameters: Δm, $m_{\rm top}$, and f, as defined in Eq. (12). The uncalibrated signal fraction $f^{\rm uncal}$ is calculated in data as an average of $f^{\rm best}$ determined at each point in the $(m_t, m_{\bar{t}})$ grid and weighted by the value of the likelihood at that point. To calibrate $f^{\rm uncal}$, we form 1000 pseudoexperiments for each input signal fraction $f^{\rm true}$ in the interval [0, 1] in increments of 0.1, and extract $f^{\rm uncal}$ for each one, following the same procedure as in data. Signal MC events with $m_t = m_{\bar{t}} = 172.5$ GeV are used for this calibration. A linear dependence is observed between $f^{\rm extr}$ and $f^{\rm true}$, where $f^{\rm extr}$ is the average of $f^{\rm uncal}$ values extracted in 1000 pseudoexperiments for a given $f^{\rm true}$. We use the results of a linear fit of $f^{\rm extr}$ to $f^{\rm true}$ to calibrate the fraction of signal events in data. The results are summarized in Table VI (see below). Possible systematic biases on the measured value of Δm from the uncertainty on f are discussed in Sec. VII.

2. Calibration of Δm

The dependence of the extracted Δm on the generated Δm is determined from the extracted values $\Delta m^{\rm extr}(m_t, m_{\bar{t}})$, again obtained from averaging $\langle \Delta m \rangle$ over 1000 pseudoexperiments for each $(m_t, m_{\bar{t}})$ combination. The resulting distribution and fit to the 14 $(m_t, m_{\bar{t}})$ points is shown in Figs. 4(a) and 4(b) for the e + jets and μ + jets channels, respectively. This provides the calibration of the extracted Δm value:

$$\Delta m^{\rm extr} = \xi_0^{\Delta m} + \xi_1^{\Delta m} \cdot \Delta m^{\rm gen}. \quad (13)$$

The fit parameters $\xi_i^{\Delta m}$ are summarized in Table IV.

For an unbiased estimate of Δm and of the uncertainty $\delta_{\Delta m}$ on the measured $\langle \Delta m \rangle$ value, the distribution of the pulls should be described by a Gaussian function with a standard deviation (SD) of unity, and centered at zero. A SD of the pulls larger than unity would indicate an underestimation of $\delta_{\Delta m}$, which could be caused by the simplifying assumptions of the ME technique discussed in Sec. V. For a given pseudoexperiment at $(m_t, m_{\bar{t}})$, we define the pull in Δm as

$$\pi_{\Delta m} = \frac{\langle \Delta m \rangle - \Delta m^{\rm extr}(m_t, m_{\bar{t}})}{\delta_{\Delta m}}. \quad (14)$$

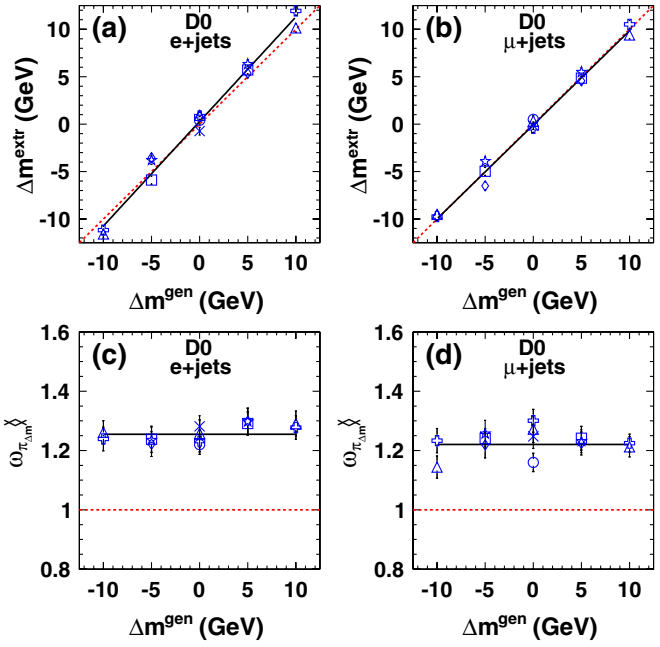

FIG. 4 (color online). The calibration of the extracted Δm value as a function of generated Δm is shown for the (a) e + jets and (b) μ + jets channels. The points are fitted to a linear function. Each point represents a set of 1000 pseudoexperiments for one of the 14 $(m_t, m_{\bar{t}})$ combinations. The circle, square, triangle, rhombus, cross, star, and "×" symbols stand for $m_{\mathrm{top}} = 165$, 167.5, 170, 172.5, 175, 177.5, and 180 GeV, respectively. Similarly, the pull widths, as defined in the text, are given for the (c) e + jets and (d) μ + jets channels.

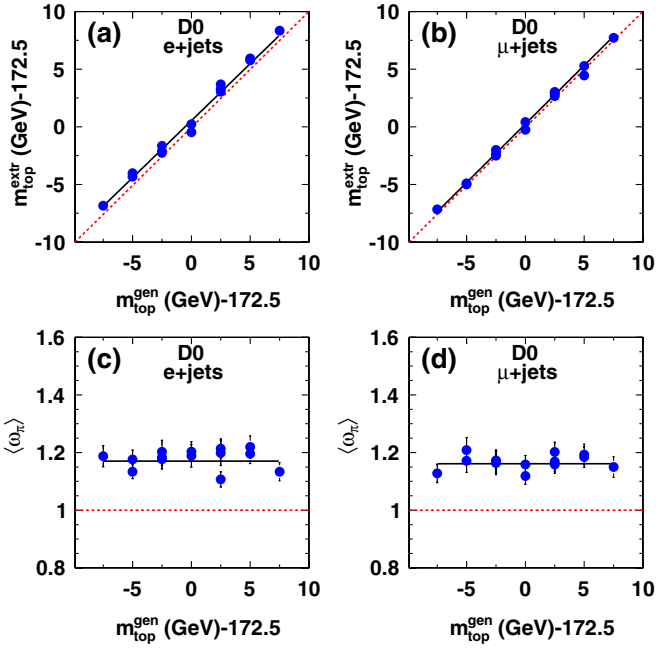

FIG. 5 (color online). The calibration of the extracted m_{top} value as a function of generated m_{top} is shown for the (a) e + jets and (b) μ + jets channels. The dependence is fitted to a linear function. Each point represents a set of 1000 pseudoexperiments for one of the 14 $(m_t, m_{\bar{t}})$ combinations. Similarly, the pull widths, as defined in the text, are given for the (c) e + jets and (d) μ + jets channels.

The pull widths $\omega_{\pi_{\Delta m}}$, defined by the SD in Gaussian fits to the pull distributions, are also shown for all 14 $(m_t, m_{\bar{t}})$ points in Figs. 4(c) and 4(d) for the e + jets and μ + jets channels, respectively. The average pull widths $\langle \omega_{\pi_{\Delta m}} \rangle$ are taken from fits of the 14 pull widths in each channel to constant offsets and are summarized in Table IV. We calibrate the estimated uncertainty according to $\delta^{\mathrm{cal}}_{\Delta m} \equiv \langle \omega_{\pi_{\Delta m}} \rangle \times \delta_{\Delta m}$.

3. Calibration of m_{top}

Results from an analogous calibration of m_{top} are displayed in Figs. 5(a) and 5(b) for the e + jets and μ + jets channels, respectively. The distributions in pull widths are given in parts (c) and (d) of the same figure. The corresponding fit parameters and average pull widths are also summarized in Table IV.

C. Results

With the calibration of Δm and m_{top}, we proceed to extract Δm and, as a cross-check, m_{top}, from the data, as described in Sec. V. As indicated previously, the probabilities for the selected events are calculated using the ME method, and the likelihoods in Δm and m_{top} are constructed independently for the e + jets and μ + jets channels.

The calibration of data involves a linear transformation of the uncalibrated axes of the likelihoods in Δm and m_{top} to their corrected values, which we denote as Δm^{cal} and $m^{\mathrm{cal}}_{\mathrm{top}}$, according to

$$\Delta m^{\mathrm{cal}} = \frac{\Delta m - \xi_0^{\Delta m}}{\xi_1^{\Delta m}}, \tag{15}$$

$$m^{\mathrm{cal}}_{\mathrm{top}} = \frac{m_{\mathrm{top}} - 172.5\ \mathrm{GeV} - \xi_0^{m_{\mathrm{top}}}}{\xi_1^{m_{\mathrm{top}}}} + 172.5\ \mathrm{GeV}, \tag{16}$$

where the ξ_i are summarized in Table IV. The resulting likelihoods for data, as a function of Δm and m_{top}, are shown in Figs. 6 and 7, respectively.

After calibration, $\langle \Delta m \rangle$ and $\langle m_{\mathrm{top}} \rangle$, with their respective uncertainties $\delta_{\Delta m}$ and $\delta_{m_{\mathrm{top}}}$, are extracted from the likelihoods as described in Sec. VI A. The uncertainties are scaled up by the average pull widths given in Table IV. The resulting distributions in expected uncertainties $\delta^{\mathrm{cal}}_{\Delta m}$ are also shown in Fig. 6.

The final measured results for Δm and m_{top} are summarized below according to channel, as well as combined:

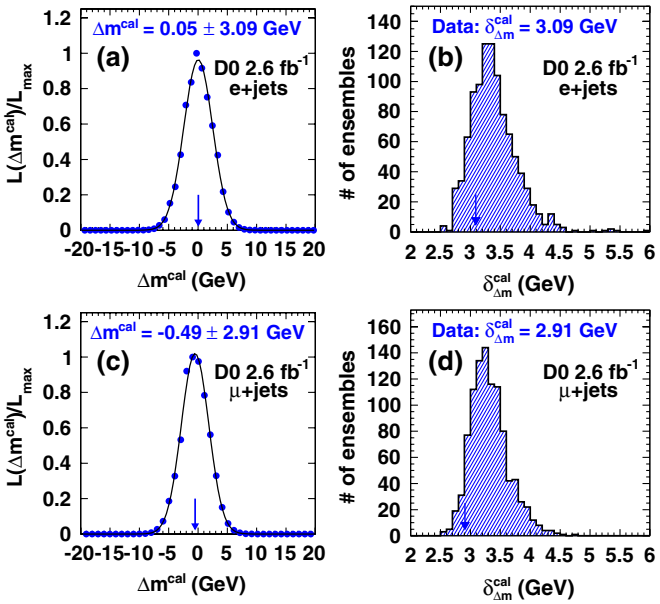

FIG. 6 (color online). The normalized likelihood in Δm^{cal} after calibration via Eq. (15), together with a Gaussian fit, is shown for the (a) e + jets and (c) μ + jets events in data. The extracted Δm^{cal} values are indicated by arrows. The distributions in expected uncertainties $\delta^{\mathrm{cal}}_{\Delta m}$ after calibration via Eq. (15) and correction for the pull width, obtained from ensemble studies using simulated MC events, are displayed for the (b) e + jets and (d) μ + jets channels. The observed $\delta^{\mathrm{cal}}_{\Delta m}$ values are indicated by arrows.

$$
\begin{aligned}
e + \text{jets}, 2.6\ \text{fb}^{-1}\text{:}\ \Delta m &= 0.1 \pm 3.1\ \text{GeV},\\
m_{\mathrm{top}} &= 173.9 \pm 1.6\ \text{GeV},\\
\mu + \text{jets}, 2.6\ \text{fb}^{-1}\text{:}\ \Delta m &= -0.5 \pm 2.9\ \text{GeV},\\
m_{\mathrm{top}} &= 175.3 \pm 1.3\ \text{GeV},\\
\ell + \text{jets}, 2.6\ \text{fb}^{-1}\text{:}\ \Delta m &= -0.2 \pm 2.1\ \text{GeV},\\
m_{\mathrm{top}} &= 174.7 \pm 1.0\ \text{GeV}.
\end{aligned}
\tag{17}
$$

The uncertainties given thus far are purely statistical. The combined ℓ + jets results are obtained by using the canonical weighted average formulas assuming Gaussian uncertainties. We cross-check the above values for m_{top} with those obtained from the absolute top quark mass analysis [43,47] and find them to be consistent.

As an additional cross-check, we independently extract the masses of the top and antitop quarks from the same data sample. The two-dimensional likelihood densities, as functions of m_t and $m_{\bar{t}}$, are displayed in Fig. 8. Also shown are contours of equal probability for two-dimensional Gaussian fits to the likelihood densities, where the Gaussian functions are of the form

$$
\begin{aligned}
P(x, y) = \frac{A}{2\pi\sigma_x\sigma_y}\frac{1}{\sqrt{1-\rho^2}}\exp\Bigg\{-\frac{1}{2}\frac{1}{1-\rho^2}\Bigg[\frac{(x-\bar{x})^2}{\sigma_x^2}\\
+\frac{(y-\bar{y})^2}{\sigma_y^2}+\frac{2\rho(x-\bar{x})(y-\bar{y})}{\sigma_x\sigma_y}\Bigg]\Bigg\},
\end{aligned}
\tag{18}
$$

with $x \equiv m_t$ and $y \equiv m_{\bar{t}}$. The fits to data yield

$$
\begin{aligned}
e + \text{jets}, 2.6\ \text{fb}^{-1}\text{:}\ m_t &= 173.8 \pm 1.5\ \text{GeV},\\
m_{\bar{t}} &= 173.8 \pm 2.0\ \text{GeV},\\
\rho &= -0.02,\\
\mu + \text{jets}, 2.6\ \text{fb}^{-1}\text{:}\ m_t &= 175.2 \pm 1.8\ \text{GeV},\\
m_{\bar{t}} &= 175.5 \pm 1.5\ \text{GeV},\\
\rho &= -0.01.
\end{aligned}
\tag{19}
$$

The above uncertainties are again purely statistical; however, in contrast to Eq. (17), they are not corrected for pull widths in m_t and $m_{\bar{t}}$. The correlation coefficients ρ are consistent with the absence of correlations.

In Sec. VIII, we will combine the results for Δm summarized in Eq. (17) with the previous measurement using 1 fb^{-1} of integrated luminosity [12].

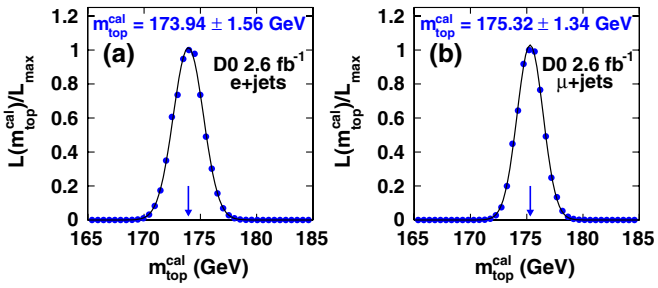

FIG. 7 (color online). The normalized likelihood in $m^{\mathrm{cal}}_{\mathrm{top}}$ after calibration via Eq. (16) together with a Gaussian fit for the (a) e + jets and (b) μ + jets channels. Arrows indicate the extracted $m^{\mathrm{cal}}_{\mathrm{top}}$ values.

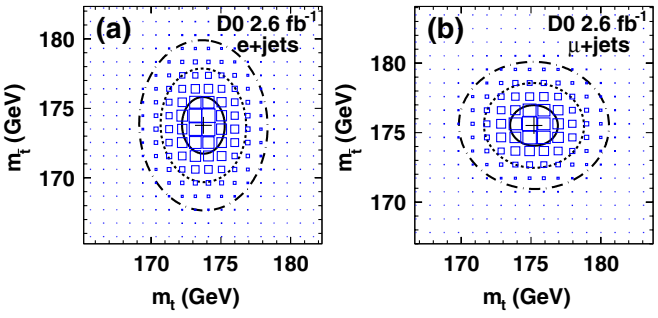

FIG. 8 (color online). Two-dimensional likelihood densities in m_t and $m_{\bar{t}}$ for the (a) e + jets and (b) μ + jets channels. The bin contents are proportional to the area of the boxes. The solid, dashed, and dash-dotted lines represent the 1, 2, and 3 SD contours of two-dimensional Gaussian fits (corresponding to approximately 40%, 90%, and 99% confidence levels, respectively) to the distributions defined in Eq. (18), respectively.

VII. SYSTEMATIC UNCERTAINTIES

For the measurement of $m_{\rm top}$ we typically consider three main types of sources of systematic uncertainties [43]: (i) modeling of $t\bar{t}$ production and background processes, (ii) modeling of detector response, and (iii) limitations inherent in the measurement method. However, in the context of a Δm measurement, many systematic uncertainties are reduced because of correlations between the measured properties of top and antitop quarks, such as the uncertainty from the absolute JES calibration. Given the small value of the upper limit of $O(5\%)$ already observed for $|\Delta m|/m_{\rm top}$, several other sources of systematic uncertainties relevant in the measurement of $m_{\rm top}$, such as modeling of hadronization, are not expected to contribute to Δm because they would affect t and $\bar{t}$ in a similar manner. Following [48], we check for any effects on Δm that might arise from sources in the latter category in Sec. VII C, and find them consistent with having no significant impact. We therefore do not consider them further in the context of this measurement. On the other hand, we estimate systematic uncertainties from additional sources which are not considered in the $m_{\rm top}$ measurement, for example, from the asymmetry in calorimeter response to b and $\bar{b}$ quark jets.

Typically, to propagate a systematic uncertainty on some parameter to the final result, that parameter is changed in the simulation used to calibrate the ME method, and the Δm result is rederived. If the change in a parameter can be taken into account through a reweighting of events, a new calibration is determined using those weights and applied directly to data. When this procedure is not possible, a reevaluation of event probabilities is performed for one sample of $t\bar{t}$ MC events corresponding to a particular choice of m_t and $m_{\bar{t}}$ closest to the most likely value according to our measurement, i.e. $m_t = m_{\bar{t}} = 175$ GeV, or, when no such sample of MC events with a changed parameter is available, $m_t = m_{\bar{t}} = 172.5$ GeV. Consequently, the results of ensemble studies are compared to those found for the default sample for the same values of m_t and $m_{\bar{t}}$.

The systematic uncertainties are described below and summarized in Table V. The total systematic uncertainty is obtained by adding all contributions in quadrature.

A. Modeling of detector

(i) *Jet energy scale:* As indicated in Sec. VI C, we use the absolute JES calibration of $k_{\rm JES} = 1.018 \pm 0.008$ determined from data. To propagate this uncertainty to Δm, we scale the jet energies in the selected data sample by $k_{\rm JES} \pm 1$ SD.

(ii) *Remaining jet energy scale:* The systematic uncertainty on the absolute JES discussed above does not account for possible effects from uncertainties on jet energy corrections that depend on $E_{\rm jet}$ and $\eta_{\rm jet}$. To estimate this effect on Δm, we rescale the energies of jets in the default $t\bar{t}$ MC sample by a differential scale factor $S(E_{\rm jet}, \eta_{\rm jet})$ that is a function of the JES uncertainties, but conserves the magnitude of the absolute JES correction.

(iii) *Response to b and light quarks:* The difference in the hadronic/electromagnetic response of the calorimeter leads to differences in the response to b and light quarks between data and simulation. This uncertainty is evaluated by rescaling the energies of jets matched to b quarks in the default $t\bar{t}$ MC sample.

(iv) *Response to b and $\bar{b}$ quarks:* The measurement of Δm can be affected by differences in the reconstruction of the transverse momenta of particles and antiparticles. A difference could, in principle, be caused by different p_T scales for μ^+ and μ^-. However, the data consist of an almost equal mix of events with opposite magnet polarities, thereby minimizing such biases. We do not observe any difference in calorimeter response to e^+ and e^-.
A systematic bias to Δm can also be caused by differences in calorimeter response to quarks and antiquarks. In the case of $t\bar{t}$ events, this bias could arise especially from a different response to b and $\bar{b}$ quarks. Several mechanisms could contribute to this, most notably a different content of K^+/K^- mesons, which have different interaction cross sections. In our evaluation of this systematic uncertainty, we assume that, although differences in response to $b/\bar{b}$ quarks are present in data, they are not modeled in MC events. We measure the difference of the calorimeter response to b quarks to that of $\bar{b}$ quarks, $\mathcal{R}_{b,\bar{b}} \equiv \mathcal{R}_b - \mathcal{R}_{\bar{b}}$, using a "tag-and-probe" method in data. Namely, we select back-to-back dijet events, and enhance the $b\bar{b}$ content by requiring b tags for both jets. The tag jet is defined by the presence of a muon within the jet cone, whose charge serves as an indication of whether the probe jet is more likely to be a b- or a $\bar{b}$-quark jet. By evaluating the $|\vec{p}_T|$ imbalance between tag-and-probe jets for positively and negatively charged muon tags, we find an upper bound $|\mathcal{R}_{b,\bar{b}}| < 0.0042$. Based on this result, we modify the default $t\bar{t}$ MC sample by rescaling the momenta $|\vec{p}|$ of b ($\bar{b}$)-quark jets by $1 \mp \frac{1}{2} \cdot \mathcal{R}_{b,\bar{b}} = 0.9979$ (1.0021), and adjusting their four-vectors accordingly. We repeat the ensemble studies after recalculating the probabilities for the modified sample and quote the difference relative to the default sample as a systematic uncertainty.

(v) *Response to c and $\bar{c}$ quarks:* A difference in calorimeter response to c and $\bar{c}$ quarks can potentially bias Δm, since c quarks appear in decays of W^+ bosons from t-quark decays, and vice versa for $\bar{c}$ and $\bar{t}$. It is experimentally difficult to isolate a sufficiently clean sample of $c\bar{c}$ dijet events, since

it will suffer from considerable contributions from $b\bar{b}$ dijet events. However, the major underlying mechanisms that could cause a response asymmetry, like, e.g., the different content of K^+/K^- mesons, are the same, but of roughly opposite magnitude between c- and b-quark jets, which would result in an anticorrelation. Based on the above, we assume the same upper bound $|\mathcal{R}_{c,\bar{c}}| \leq \mathcal{R}_{b,\bar{b}} < 0.0042$, and treat $\mathcal{R}_{c,\bar{c}}$ and $\mathcal{R}_{b,\bar{b}}$ as uncorrelated. To propagate the systematic uncertainty from $\mathcal{R}_{c,\bar{c}}$ to Δm, we apply a similar technique to that for the estimation of the systematic uncertainty due to different response to b and $\bar{b}$ quarks.

(vi) *Jet identification efficiency:* D0 uses scale factors to achieve data/MC agreement in jet identification efficiencies. To propagate to the Δm measurement the effect of uncertainties on these scale factors, we decrease the jet identification efficiencies in the default $t\bar{t}$ sample according to their uncertainties.

(vii) *Jet energy resolution:* An additional smearing of jet energies derived by comparison of the p_T balance in $(Z \rightarrow ee) + 1$ jet events [49] is applied to all MC samples in this analysis in order to achieve better data/MC agreement. To evaluate any effect from data/MC disagreement in jet energy resolutions on Δm, we modify the default $t\bar{t}$ MC sample by varying the jet energy resolution within its uncertainty.

(viii) *Determination of lepton charge:* This analysis uses the charge of the lepton in $t\bar{t}$ candidate events to distinguish the top quark from the antitop quark. Incorrectly reconstructed lepton charges can result in a systematic shift in the measurement. The charge misidentification rate is found to be less than 1% in studies of $Z \rightarrow ee$ data events. To estimate the contribution of this uncertainty, we assume a charge misidentification rate of 1% for both e + jets and μ + jets final states and evaluate the effects on Δm resulting from a change in the mean values of the extracted m_t^{cal} and $m_{\bar{t}}^{\text{cal}}$.

B. ME method

(i) *Signal fraction:* The signal fractions f presented in Table III are changed by their respective uncertainties for each decay channel, and ensemble studies are repeated for all MC samples to rederive the calibration for Δm. The new calibrations are applied to data and the results compared with those obtained using the default calibration.

(ii) *Background from multijet events:* In the calibration of this analysis, the background contribution to pseudoexperiments is formed using only W + jets events, as they are also assumed to model the small MJ background from QCD processes and smaller contributions from other background processes present in the data. To estimate the systematic uncertainty from this assumption, we define a dedicated MJ-enriched sample of events from data. The calibration is rederived with this background sample included in forming pseudoexperiments.

(iii) *Calibration of the ME method:* The statistical uncertainties associated with the offset (ξ_0) and slope (ξ_1) parameters that define the mass calibration in Sec. VI B contribute to the uncertainty on Δm. To quantify this, we calculate the uncertainty $\delta_{\Delta m}$ due to δ_{ξ_0} and δ_{ξ_1} for each channel according to the error propagation formula

$$\delta_{\Delta m} = \left\{ \left(\frac{\Delta m - \xi_0}{\xi_1^2} \cdot \delta_{\xi_1} \right)^2 + \left(\frac{\delta_{\xi_0}}{\xi_1} \right)^2 \right\}^{-(1/2)}$$

and then combine the resulting uncertainties for the e + jets and μ + jets channels in quadrature.

TABLE III. Signal fractions determined from data for the assumption that $m_t = m_{\bar{t}} = 172.5$ GeV. The uncertainties are statistical only.

Channel	Measured signal fraction
e + jets	0.71 ± 0.05
μ + jets	0.75 ± 0.04

TABLE IV. Fit parameters for the calibration of Δm and m_{top}, defined by Eq. (13), and average pull widths $\langle \omega_\pi \rangle$ for pulls in Δm and m_{top}, defined in Eq. (14).

	Channel	ξ_0 (GeV)	ξ_1	$\langle \omega_\pi \rangle$
Δm	e + jets	0.28 ± 0.14	1.10 ± 0.02	1.25 ± 0.01
	μ + jets	-0.08 ± 0.13	0.99 ± 0.02	1.22 ± 0.01
m_{top}	e + jets	0.53 ± 0.08	0.99 ± 0.02	1.17 ± 0.01
	μ + jets	0.24 ± 0.07	1.02 ± 0.02	1.16 ± 0.01

TABLE V. Summary of systematic uncertainties on Δm.

Source	Uncertainty on Δm (GeV)
Modeling of detector:	
Jet energy scale	0.15
Remaining jet energy scale	0.05
Response to b and light quarks	0.09
Response to b and $\bar{b}$ quarks	0.23
Response to c and $\bar{c}$ quarks	0.11
Jet identification efficiency	0.03
Jet energy resolution	0.30
Determination of lepton charge	0.01
ME method:	
Signal fraction	0.04
Background from multijet events	0.04
Calibration of the ME method	0.18
Total	0.47

C. Additional checks

We check for effects on Δm from sources of systematic uncertainties considered in the $m_{\rm top}$ measurement [43] which are not expected to contribute any bias in the context of the measurement of Δm. For this, we follow the same approach as outlined at the beginning of this section. We find the results of our checks to be indeed consistent with no bias on Δm.

The additional checks are described below and summarized in Table VI. Note that the numbers quoted merely reflect an upper bound on a possible bias, rather than any true effect. This limitation is statistical in nature and due to the number of available simulated MC events. Furthermore, if the difference between the central result and the one obtained for a check is smaller than the statistical uncertainty on this difference, we quote the latter.

1. Modeling of physical processes

(i) *Higher-order corrections:* To check the effect of higher-order corrections on Δm, we perform ensemble studies using $t\bar{t}$ events generated with (i) the NLO MC generator MC@NLO [50], and (ii) the LO MC generator ALPGEN, with HERWIG [51] for hadronization and shower evolution.

(ii) *Initial- and final-state radiation:* The modeling of extra jets from ISR/FSR is checked by comparing PYTHIA samples with modified input parameters, such as the ± 1 SD changes, found in a study of Drell-Yan processes [52].

(iii) *Hadronization and underlying event:* To check a possible effect of Δm from the underlying event as well as the hadronization models, we compare samples hadronized using PYTHIA with those hadronized using HERWIG.

(iv) *Color reconnection:* The default PYTHIA tune used at D0 (tune A), does not include explicit color reconnection. For our check, we quantify the difference between Δm values found in ensemble studies for $t\bar{t}$ MC samples generated using tunes Apro and ACRpro, where the latter includes an explicit model of color reconnection [53,54].

(v) *b fragmentation:* Uncertainties in the simulation of b-quark fragmentation can affect the measurement of $m_{\rm top}$ in several phases of the analysis, such as in b tagging and in the b-quark transfer functions used in the ME calculations. Such effects are studied in the context of Δm by reweighting the simulated $t\bar{t}$ events used in the calibration of the method from the default Bowler scheme [55], which is tuned to LEP (ALEPH, OPAL, and DELPHI) data, to a tune that accounts for differences between SLD and LEP data [56].

(vi) *Uncertainty on PDF:* The CTEQ6M [33] PDFs provide a set of possible excursions in parameters from their central values. To check the effect on Δm from PDFs, we change the default $t\bar{t}$ MC sample (generated using CTEQ6L1) by reweighting it to CTEQ6M, repeat the ensemble studies for each of the parameter variations, and evaluate the uncertainty using the prescribed formula [33]:

$$\delta_{\Delta m,\mathrm{PDF}} = \frac{1}{2}\left\{\sum_{i=1}^{20}[\Delta m(S_i^+) - \Delta m(S_i^-)]^2\right\}^{1/2},$$

where the sum runs over PDF uncertainties for positive (S_i^+) and negative (S_i^-) excursions.

(vii) *Multiple hadron interactions:* When calibrating the ME method, we reweight the luminosity profiles of our MC samples to the instantaneous luminosity profile for that data-taking period. For our check, we rederive the calibration, ignoring luminosity-dependent weights.

(viii) *Modeling of background:* We check the effect of inadequate modeling of background processes on our Δm measurement by identifying distributions in the background-dominated $\ell + 3$ jets events that display only limited agreement between data and predictions from the sum of our signal and background models, as determined through a Kolmogorov-Smirnov test [57]. The calibration of the method is then redone using W + jets events that are reweighted to bring the identified distributions of predicted signal and background events into better agreement with data.

TABLE VI. Summary of additional checks for a possible bias on Δm. None of those show any significant bias on Δm. Note that the numbers shown reflect an upper limit on a possible bias. This limitation is of statistical origin and due to the number of available simulated MC events.

Source	Change in Δm (GeV)
Modeling of physical processes:	
Higher-order corrections	0.26
ISR/FSR	0.21
Hadronization and underlying event	0.23
Color reconnection	0.27
b fragmentation	0.03
PDF uncertainty	0.10
Multiple hadron interactions	0.06
Modeling of background	0.07
Heavy-flavor scale factor	0.02
Modeling of detector:	
Trigger selection	0.07
b-tagging efficiency	0.25
Momentum scale for e	0.05
Momentum scale for μ	0.06

(ix) *Heavy-flavor scale factor:* As discussed in Sec. IV, a heavy-flavor scale factor of 1.47 ± 0.22 is applied to the $W + b\bar{b}$ + jets and $W + c\bar{c}$ + jets production cross sections to increase the heavy-flavor content in the ALPGEN W + jets MC samples. Moreover, a scale factor of 1.27 ± 0.15 for the $W + c$ + jets production cross section is obtained using MCFM. We rederive the calibration with the heavy-flavor scale factor changed by $\pm 30\%$ to check the magnitude of the effect on Δm.

2. Modeling of detector

(i) *Trigger selection:* To check the magnitude of the effect from differential trigger efficiencies on Δm, we rederive a new Δm calibration ignoring the trigger weights.

(ii) *b-tagging efficiency:* We check the possibility of a bias in our Δm measurement from discrepancies in the b-tagging efficiency between data and MC events by using *absolute* uncertainties on the b-tagging efficiencies, and account independently for possible discrepancies that are *differential* in η and p_T of the jet by reweighting the b-tagging rate in simulated $t\bar{t}$ MC events to that observed in data. The total magnitude of a possible effect is determined by combining in quadrature excursions of Δm values obtained with the modified calibrations for both absolute and differential changes.

(iii) *Momentum scale for electrons:* D0 calibrates the energy of electrons based on studies of the $Z \to ee$ mass for data and MC events. We rescale the electron energies in the default signal MC sample according to the uncertainties on the electron energy calibration to check the magnitude of the effect in the context of Δm.

(iv) *Momentum scale for muons:* The absolute momentum scale for muons is obtained from $J/\psi \to \mu\mu$ and $Z \to \mu\mu$ data. However, both linear and quadratic interpolation between these two points can be employed for the calibration. We check the effect of each extrapolation on Δm by applying the respective corrections to simulated $t\bar{t}$ MC events in the default sample, and find a larger shift in Δm for the linear parametrization.

VIII. COMBINING THE 2.6 fb^{-1} AND 1 fb^{-1} ANALYSES

We use the best linear unbiased estimator (BLUE) method [58,59] to combine our new measurement [Eq. (17)] with the result of the analysis performed on data corresponding to 1 fb^{-1} [12]. The BLUE method assumes Gaussian uncertainties and accounts for correlations among measurements. For reference, we summarize the results obtained for 1 fb^{-1}:

e + jets, 1 fb^{-1}: $\Delta m = 0.3 \pm 5.0$(stat) GeV,

μ + jets, 1 fb^{-1}: $\Delta m = 6.7 \pm 4.7$(stat) GeV,

ℓ + jets, 1 fb^{-1}: $\Delta m = 3.8 \pm 3.4$(stat) GeV.

The 1 fb^{-1} analysis used a data-driven method to estimate systematic uncertainties from modeling of signal processes. This method did not distinguish between different sources of systematic uncertainties such as (i) higher-order corrections, (ii) initial- and final-state radiation, (iii) hadronization and the underlying event, and (iv) color reconnection. The above sources are studied in the context of the m_{top} measurement [43], but are not expected to contribute any bias to the measurement of Δm. We cross-check their impact on Δm in Sec. VII C, and find them consistent with no bias. Based on our findings, we do not consider any systematic uncertainties from modeling of signal and background processes.

Two sources of systematic uncertainties from modeling of detector performance (Table V) are taken to be uncorrelated between the two measurements: JES and remaining JES. The rest are taken to be fully correlated.

In the 1 fb^{-1} analysis, a systematic uncertainty of 0.4 GeV from the difference in calorimeter response to b and $\bar{b}$ quarks was estimated using MC studies and checks in data. This systematic uncertainty has been reevaluated using an entirely data-driven approach [item (iv) in Sec. VII A], and we therefore use this new result for the analysis of the 1 fb^{-1} data. Furthermore, we now evaluate a systematic uncertainty from the difference in calorimeter response to c and $\bar{c}$ quarks, and propagate our findings to the 1 fb^{-1} analysis.

All other systematic uncertainties not explicitly mentioned above are taken as uncorrelated.

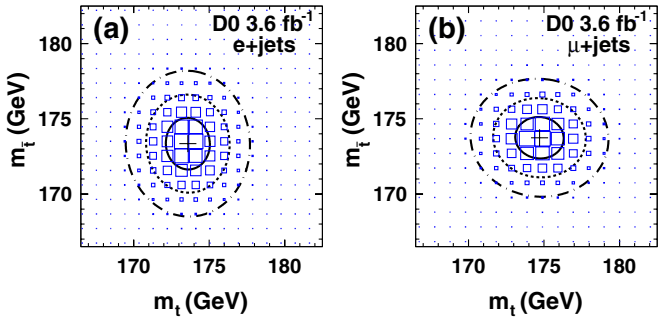

FIG. 9 (color online). Combined likelihoods of the 2.6 fb^{-1} and 1 fb^{-1} measurements as functions of m_t and $m_{\bar{t}}$ in data for the (a) e + jets and (b) μ + jets channels. The bin contents are proportional to the area of the boxes. The solid, dashed, and dash-dotted lines represent the 1, 2, and 3 SD contours of two-dimensional Gaussian fits defined in Eq. (18) (corresponding to approximately 40%, 90%, and 99% confidence levels, respectively) to the distributions, respectively. No pull corrections have been applied, and therefore the figures are for illustrative purposes only.

The combined result for Δm corresponding to 3.6 fb^{-1} of data is

$$\Delta m = 0.84 \pm 1.81(\text{stat}) \pm 0.48(\text{syst}) \text{ GeV}. \quad (26)$$

In this combination, BLUE determines a relative weight of 72.8% (27.2%) for the 2.6 fb^{-1} (1 fb^{-1}) measurement. The χ^2/N_{DOF} of the combination is 0.96. The combined likelihood densities for the two analyses are presented in Fig. 9 as functions of m_t and $m_{\bar{t}}$, separately for the e + jets and μ + jets channels.

IX. CONCLUSION

We have applied the matrix element method to the measurement of the mass difference Δm between top and antitop quarks using $t\bar{t}$ candidate events in the lepton + jets channel in data corresponding to an integrated luminosity of about 3.6 fb^{-1}. We find

$$\Delta m = 0.8 \pm 1.8(\text{stat}) \pm 0.5(\text{syst}) \text{ GeV},$$

which is compatible with no mass difference at the level of $\approx 1\%$ of the mass of the top quark.

ACKNOWLEDGMENTS

We thank the staffs at Fermilab and collaborating institutions, and acknowledge support from the DOE and NSF (USA); CEA and CNRS/IN2P3 (France); FASI, Rosatom, and RFBR (Russia); CNPq, FAPERJ, FAPESP, and FUNDUNESP (Brazil); DAE and DST (India); Colciencias (Colombia); CONACyT (Mexico); KRF and KOSEF (Korea); CONICET and UBACyT (Argentina); FOM (The Netherlands); STFC and the Royal Society (United Kingdom); MSMT and GACR (Czech Republic); CRC Program and NSERC (Canada); BMBF and DFG (Germany); SFI (Ireland); The Swedish Research Council (Sweden); and CAS and CNSF (China).

APPENDIX: GENERATION OF $t\bar{t}$ EVENTS WITH $M_t \neq M_{\bar{t}}$

We briefly describe below the modifications to the standard PYTHIA [32] code which were necessary to generate $t\bar{t}$ events with $m_t \neq m_{\bar{t}}$. A new entry in the KF particle table is created for the $\bar{t}$ quark. The PYINPR subroutine is modified for use cases in which one of the $t\bar{t}$ production subprocesses (ISUB = 81, 82, 84, 85) is called. The $\bar{t}$ quark is assigned as the second final-state particle whenever a t quark is selected as the first final-state particle. Furthermore, the ordering of the first and second final-state particles is swapped, as needed, in the subroutine PYSCAT. Additional changes are made in the subroutines PYMAXI, PYRAND, and PYRESD to set the lower limit on the combined masses of the W^+ (W^-) boson and b ($\bar{b}$) quark to the t ($\bar{t}$) quark mass. Finally, the subroutine PYWIDT is modified to adjust the resonance widths Γ_t and $\Gamma_{\bar{t}}$ as functions of m_t and $m_{\bar{t}}$.

[1] J. Schwinger, Phys. Rev. **82**, 914 (1951).
[2] G. Luders, K. Dan. Vidensk. Selsk. Mat. Fys. Medd. **28**, 5 (1954).
[3] *Niels Bohr and the Development of Physics*, edited by W. Pauli (McGraw-Hill, New York, 1955), p. 30.
[4] J. S. Bell, Proc. R. Soc. A **231**, 479 (1955).
[5] D. Colladay and V. A. Kostelecky, Phys. Rev. D **55**, 6760 (1997).
[6] O. W. Greenberg, Phys. Rev. Lett. **89**, 231602 (2002).
[7] K. Nakamura *et al.* (Particle Data Group), J. Phys. G **37**, 075021 (2010).
[8] J. A. R. Cembranos, A. Rajaraman, and F. Takayama, Europhys. Lett. **82**, 21001 (2008).
[9] F. Abe *et al.* (CDF Collaboration), Phys. Rev. Lett. **74**, 2626 (1995).
[10] S. Abachi *et al.* (D0 Collaboration), Phys. Rev. Lett. **74**, 2632 (1995).
[11] Tevatron Electroweak Working Group, arXiv:1007.3178.
[12] V. M. Abazov *et al.* (D0 Collaboration), Phys. Rev. Lett. **103**, 132001 (2009).
[13] V. M. Abazov *et al.* (D0 Collaboration), Phys. Rev. D **74**, 092005 (2006).
[14] V. M. Abazov *et al.* (D0 Collaboration), Phys. Rev. Lett. **101**, 182001 (2008).
[15] K. Kondo, J. Phys. Soc. Jpn. **57**, 4126 (1988).
[16] R. H. Dalitz, G. R. Goldstein, and K. Sliwa, Phys. Rev. D **47**, 967 (1993).
[17] R. H. Dalitz and G. R. Goldstein, Proc. R. Soc. A **455**, 2803 (1999).
[18] V. M. Abazov *et al.* (D0 Collaboration), Nature (London) **429**, 638 (2004).
[19] T. Aaltonen *et al.* (CDF Collaboration), Phys. Rev. Lett. **106**, 152001 (2011).
[20] V. M. Abazov *et al.* (D0 Collaboration), Nucl. Instrum. Methods Phys. Res., Sect. A **565**, 463 (2006).
[21] R. Angstadt *et al.*, Nucl. Instrum. Methods Phys. Res., Sect. A **622**, 298 (2010).
[22] The previous measurement in Ref. [12] is based on data corresponding to 1 fb^{-1} of integrated luminosity recorded before the installation of layer 0, while the new measurement presented here is based on data corresponding to 2.6 fb^{-1} of integrated luminosity recorded after this installation.
[23] D0 uses a cylindrical coordinate system with the z axis running along the proton beam axis. The angles θ and ϕ are the polar and azimuthal angles, respectively. Rapidity y and pseudorapidity η are defined as functions of the polar angle θ and parameter β as $y(\theta, \beta) \equiv \frac{1}{2}\ln[(1 + \beta\cos\theta)/(1 - \beta\cos\theta)]$ and $\eta(\theta) \equiv y(\theta, 1)$, where β is the ratio of a particle's momentum to its

energy. Throughout, we define η with respect to the center of the detector.

[24] The transverse impact parameter is defined as the distance of closest approach (dca) of the track to the PV in the plane transverse to the beam line. Its significance is defined as dca/δdca, where δdca is the uncertainty on dca.

[25] S. Abachi *et al.* (D0 Collaboration), Nucl. Instrum. Methods Phys. Res., Sect. A **338**, 185 (1994).

[26] V. M. Abazov *et al.* (D0 Collaboration), Nucl. Instrum. Methods Phys. Res., Sect. A **552**, 372 (2005).

[27] M. Abolins *et al.*, Nucl. Instrum. Methods Phys. Res., Sect. A **584**, 75 (2008).

[28] G. C. Blazey *et al.*, in *Proceedings of the Workshop "QCD and Weak Boson Physics in Run II,"* edited by U. Baur, R. K. Ellis, and D. Zeppenfeld (Fermilab, Batavia, IL, 2000), p. 47; see Sec. 3.5 for details, arXiv:hep-ex/0005012.

[29] V. M. Abazov *et al.* (D0 Collaboration), Phys. Rev. D **76**, 092007 (2007).

[30] V. M. Abazov *et al.* (D0 Collaboration), Nucl. Instrum. Methods Phys. Res., Sect. A **620**, 490 (2010).

[31] R. Brun and F. Carminati, CERN Program Library Long Writeup W5013, CERN, Geneva, 1993.

[32] T. Sjöstrand *et al.*, J. High Energy Phys. 05 (2006) 026.

[33] J. Pumplin *et al.*, J. High Energy Phys. 07 (2002) 012; D. Stump *et al.*, J. High Energy Phys. 10 (2003) 046.

[34] M. L. Mangano, M. Moretti, F. Piccinini, R. Pittau, and A. D. Polosa, J. High Energy Phys. 07 (2003) 001.

[35] M. L. Mangano, M. Moretti, F. Piccinini, and M. Treccani, J. High Energy Phys. 01 (2007) 013.

[36] J. M. Campbell and R. K. Ellis, Nucl. Phys. B, Proc. Suppl. **205-206**, 10 (2010).

[37] E. Boos *et al.* (CompHEP Collaboration), Nucl. Instrum. Methods Phys. Res., Sect. A **534**, 250 (2004).

[38] D0 tune A is identical to tune A [39], but uses the CTEQ6L1 PDF set and sets $\Lambda_{\mathrm{QCD}} = 0.165$ GeV.

[39] T. Affolder *et al.* (CDF Collaboration), Phys. Rev. D **65**, 092002 (2002).

[40] V. M. Abazov *et al.* (D0 Collaboration), Phys. Rev. D **76**, 092007 (2007).

[41] S. Moch and P. Uwer, Phys. Rev. D **78**, 034003 (2008).

[42] J. Smith, W. L. van Neerven, and J. A. M. Vermaseren, Phys. Rev. Lett. **50**, 1738 (1983).

[43] V. M. Abazov *et al.* (D0 Collaboration), Phys. Rev. D **84**, 032004 (2011).

[44] G. Mahlon and S. J. Parke, Phys. Lett. B **411**, 173 (1997).

[45] F. A. Berends *et al.*, Nucl. Phys. **B357**, 32 (1991).

[46] R. Barlow, Report No. MAN/HEP/99/4, 2000.

[47] To check the consistency, our measured value of m_{top} is to be compared with that found in Ref. [43], but before applying the sample-dependent corrections described in Sec. VII of Ref. [43]. These corrections produce shifts of $\Delta m_{\mathrm{top}} = 1.26$ GeV and $\Delta k_{\mathrm{JES}} = -0.005$. Hence, the values of m_{top} from our analysis serve only as cross-checks, whereas the final result in Ref. [43] includes all the relevant corrections.

[48] R. Barlow, arXiv:hep-ex/0207026.

[49] C. Ochando, Ph.D. thesis, Fermilab [Report No. FERMILAB-THESIS-2008-78, 2008].

[50] S. Frixione and B. R. Webber, J. High Energy Phys. 06 (2002) 029.

[51] G. Corcella *et al.*, J. High Energy Phys. 01 (2001) 010; arXiv:hep-ph/0210213.

[52] A. Abulencia *et al.* (CDF Collaboration), Phys. Rev. D **73**, 032003 (2006).

[53] P. Z. Skands and D. Wicke, Eur. Phys. J. C **52**, 133 (2007).

[54] A. Buckley *et al.*, Eur. Phys. J. C **65**, 331 (2009).

[55] M. G. Bowler, Z. Phys. C **11**, 169 (1981).

[56] Y. Peters, K. Hamacher, and D. Wicke, Report No. FERMILAB-TM-2425-E, 2009.

[57] A. Kolmogorov, G. Inst. Ital. Attuari **4**, 83 (1933); N. V. Smirnov, Ann. Math. Stat. **19**, 279 (1948).

[58] L. Lyons, D. Giabut, and P. Cliffort, Nucl. Instrum. Methods Phys. Res., Sect. A **270**, 110 (1988).

[59] A. Valassi, Nucl. Instrum. Methods Phys. Res., Sect. A **500**, 391 (2003).